1

Introduction to Persistently Luminescent Materials

Nimai Pathak[1,2] and Yuanbing Mao[1]

[1] Illinois Institute of Technology, Department of Chemistry, 3101 S Dearborn Street, Chicago, IL 60616, USA
[2] Bhabha Atomic Research Centre, Radiochemistry Division, Central Avenue Road, Trombay, Mumbai, Maharashtra, 400085, India

1.1 Introduction

The term "persistent luminescence" (hereinafter PersL) generally refers to the glow-in-the-dark or the "afterglow" property of a light emitting material, which continuously emits light lasting for a relatively long time, starting from seconds to even days after ceasing the excitation sources like ultraviolet (UV) or visible light (visible light in rare cases), electron beams, or high energy radiation such as X-, α-, β-, or γ-rays. It has a rich history which can be traced back as long as 1000 years ago when a Chinese artist Z. Xu painted a cow resting inside a barn with a special "night-vision" ink imported from Japan. This inexplicable magic was later described by Y. Wen in a Chinese miscellaneous note called "Xiāng Shán Yě Lù" in the ancient Song dynasty (960–1279 CE) [1–3]. There was no scientific evidence about the raw material used for the preparation of this special "night-vision" ink, but it was possibly sulfide compounds made of calcium from pearl shells and sulfur from volcanic activities [4]. Although most of the literature on persistently luminescent materials (PLMs) were available since the beginning of twenty-first century (Figure 1.1a and c), a well-organized report on any such night-vision PLM substance was first written on Bologna stone by O. Montalbani in the book "De Illuminabili Lapide Bononiensi Epistola" in 1634 and then by F. Licetus in the book "Litheosphorus Sive de Lapide Bononiensi" in 1640 as shown in Figure 1.1b [2, 4]. An orange and reddish afterglow was observed from this stone in the dark after prior illumination by either sunlight or flame and described as "golden light of the Sun." The stone was first synthesized by the Italian alchemist V. Cascariolo by calcining the mineral barite ($BaSO_4$), found in Bologna, Italy. This marked the beginning of modern luminescence materials. The word "luminescence" was firstly used by E. Wiedemann, a German physicist in 1888, originating from the Latin word lumen with the meaning of light [6].

Limited research was carried out to develop new afterglow materials until the end of the twentieth century. It took ~400 years to prove that, instead of any "magic"

Persistently Luminescent Materials: From Development to Applications, First Edition.
Edited by Yuanbing Mao.

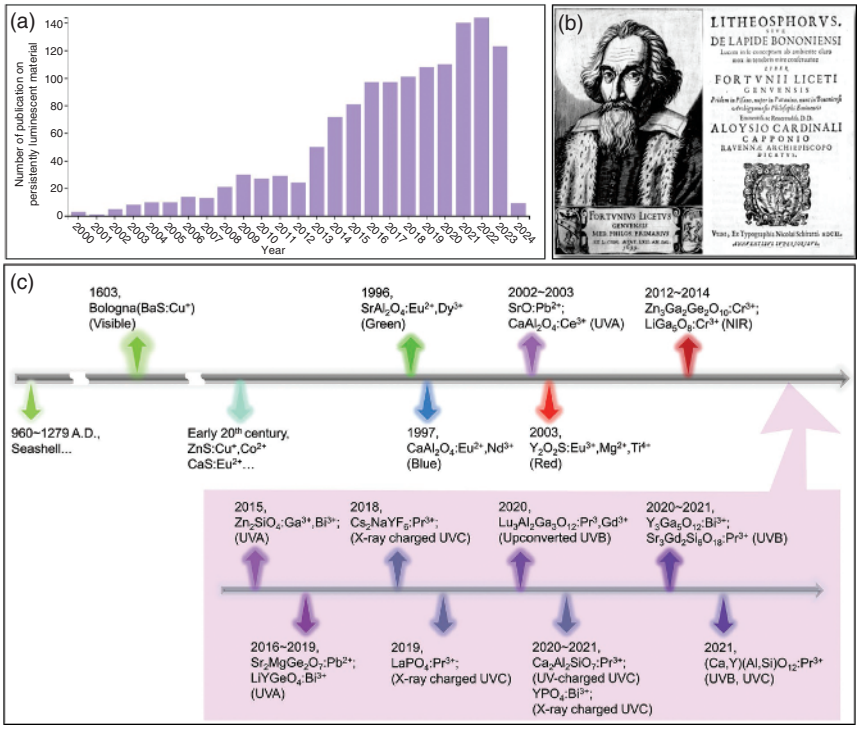

Figure 1.1 (a) Number of publications on PLMs in the Web of Science. (b) The book "Litheosphorus Sive de Lapide Bononiensi" about the afterglow phenomenon of the Bologna stone written by Fortunius Licetus in 1640 (Bologna, Italy). Source: Adapted from Yuan [5]. (c) History of the development of PLMs. Source: Yuan [5]/IOP Publishing.

power, the $3d^9 4s^1 \rightarrow 3d^{10}$ transition of Cu^+ impurities present in the Bologna stone is responsible for reddish-orange afterglow peaking at ~610 nm in the year 2012 [6]. For about 130 years, zinc sulfide (ZnS) doped with copper (Cu^+) and codoped with cobalt (Co^{2+}) emitting green emission (~530 nm) was dominating commercial afterglow materials. It was particularly used in the military during World War I and World War II as well as for various civilian purposes such as luminous paints, watch dials, and "glow-in-the-dark" toys, among others [2, 3, 7, 8]. Later on, trace amount of radioactive elements such as radium (Ra), promethium (Pm), or tritium (^3H) were introduced into ZnS:Cu^+,Co^{2+} system in order to improve its weak brightness and short persistency of luminescence. Although continuous irradiation by α- or β-rays due to radioactive decay of those radioisotopes helped to improve the light output [4], the use of radioactive materials became a huge public concern in late 1990 owing to their unavoidable health problems and environmental pollution [4, 9]. This resulted in a sharp decrease in the annual sales of watches made of radioactive LPPs. Later, considering the huge potential market of watches based on PLMs, Japanese company Nemoto & Co., Ltd. gave a specific focus on developing radioactive-free afterglow phosphors. After much trial and error, they finally succeeded in 1996 in

developing the new generation PLM of $SrAl_2O_4:Eu^{2+},Dy^{3+}$ with a bright green emission peaking at ~520 nm and lasted for over 30 hours [10–12]. Since the development of $SrAl_2O_4:Eu^{2+},Dy^{3+}$ PLM, the searching for various other novel PLMs began to speed up around the world.

Most of the PLMs developed before and after the discovery of $SrAl_2O_4:Eu^{2+},Dy^{3+}$ are inorganic in nature as discussed in Section 1.3.2. Molecular organic solid-state materials with persistent luminescence, originated from room temperature phosphorescence (RTP) and thermally activated delayed fluorescence (TADF), are also becoming increasingly popular. Molecular PLMs (MPLMs) have several advantages over their inorganic counterparts containing transition metals and/or rare earth metals, such as potentially facile tuning of structure, simple processing, and easy fabrication of soft and flexible optical devices. They have shown potential applications in biological imaging, optical recording devices, chemical sensing, and security systems [13–15]. However, many scientific and technical issues still remain to be resolved before their widespread implementations. For instance, their optical properties are highly dependent on their crystalline state and need to be used in the solid state because their solution or amorphous forms show weak persistent luminescence. PersL based on molecular hybrid structures can overcome these limitations because intermolecular interactions such as hydrogen bonding enhance the rigidity of molecular conformations and restrict molecular motions and vibration. This helps to minimize the nonradiative decay of triplet excitons and improve their photoemission lifetimes and quantum efficiencies (QEs) [14]. As studies on MPLMs have been advanced tremendously in recent years, inorganic PLMs (IPLMs) have been investigated more in both research and development. Hence, we have mostly focused discussion on IPLMs with limited examples of MPLMs in this chapter as well as this book.

So far applications of IPLMs such as LumiNova® products are mostly in the areas of decoration, toys, safety signage, watch dials, and displays (Figure 1.2a–f). Continuous efforts have been put into exploring their new applications, such as glow-in-the-dark road markings, bio-imaging, photocatalysis, AC-driven light-emitting diodes (LEDs) with reduced flickering, or pressure sensors to visualize ultrasound beams [18–21]. Research work on these new applications has progressed well while many challenges are still facing as shown in Figure 1.2e. In other words, after the successful development of the bright green emitting $SrAl_2O_4:Eu^{2+},Dy^{3+}$ PLM, research interest and effort on both finding new and efficient PLMs and exploring their potential applications on various advanced fields have been significantly increased as suggested by hundreds of new publications reported yearly on various PLMs as shown in Figure 1.1a. Hence, many review papers, book chapters, and sometimes entire books have been published on PLMs to cover the whole field, focused on a specific class of materials including Eu^{2+}, Cr^{3+}, and Mn^{2+}-doped PLMs, or targeted specific applications like near-infrared (NIR) bio-imaging by researchers worldwide [5, 12, 16, 17, 22–27]. Most of these publications introduce key synthesis methods, characterization methods, physical mechanisms, and applications of this important luminescent materials system. They cover mostly the basics of PersL followed with a concise description of the

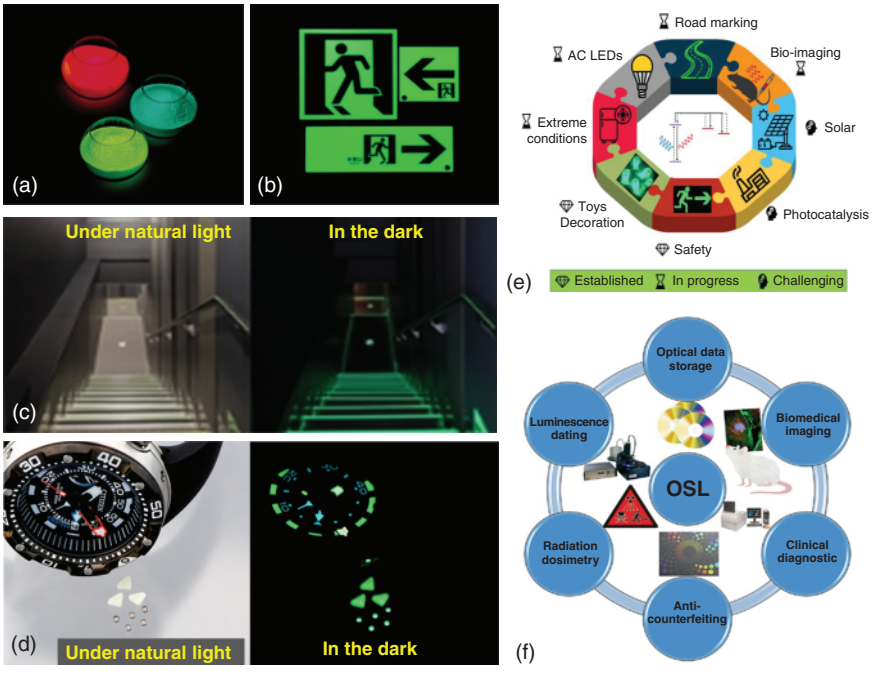

Figure 1.2 (a) Examples of LumiNova® products and their practical usages for (b) emergency signage, (c) "night-vision" luminous paints, and (d) watch dials. Source: [16]/Nemoto & Co., Ltd. (e) A summary of various established, in progress, and challenging applications of PLMs. Source: Poelman et al. [17]/AIP Publishing. (f) Applications of PLMs based on optically stimulated luminescence. Source: Adapted from Yuan [5].

most relevant applications of related PLMs. To advance PersL and PLMs to the next stage, we dedicate this book to the perspective of practical needs related to the applications of PLMs, which is expected to attract a broader readership, including not just specialists and professionals in the field, but also extending to beginners to this diverse field along with any interested parties to this fascinating field.

With this intention in mind, in this introductory (Chapter 1), we provide a brief description of various PLMs, the basic mechanism involved in PersL in both inorganic and organic PLMs, various synthesis methods for making PLMs, main characterization techniques for PersL properties, and trap manipulation for improving PersL of PLMs. This chapter is helpful for readers to brush up their background knowledge of PersL and PLMs. It provides some fundamental guidelines for future development of efficient PLMs before introducing other chapters in this book which are focused on various advanced applications of PLMs, specifically, advances in the applications of long persistent phosphors in display technology field of long persistent phosphor (Chapter 2), persistent luminescence-based LEDs (Chapter 3), persistently luminescent nanoparticles for bioimaging and biosensors (Chapter 4), persistently luminescent nanoparticles for cancer therapy (Chapter 5), persistently luminescent inorganic materials for anticounterfeiting (Chapter 6), recent advances

of the deep trap persistent phosphor for optical data storage (Chapter 7), afterglow thermometer using persistent phosphors (Chapter 8), and persistent luminescence and applications of molecular materials and their hybrids (Chapter 9).

1.2 PersL Processes and Emission Mechanisms

It is now widely accepted and well supported by mounting evidence that various defects or impurity-related traps inside the band gap of material play the crucial role of trapping excited electrons or holes followed by a delay in the electron–hole recombination and are responsible for luminescence lasting from several seconds to hours. As the simple pictorial representation is given in Figure 1.3a, during a

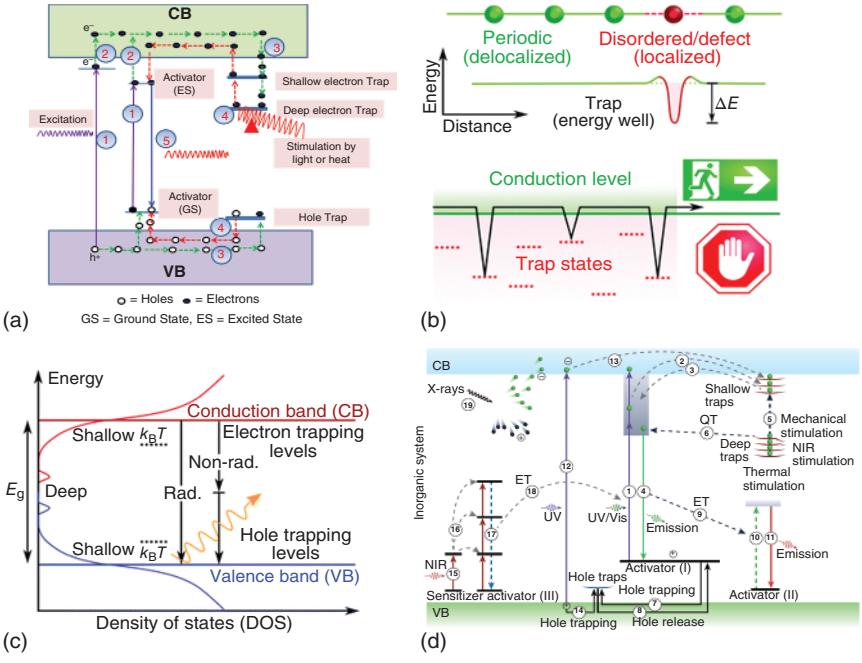

Figure 1.3 (a) Basic steps of PersL process: (1) excitation of electrons, (2) photoionization of electrons into CB, (3) trapping of the excited electrons and holes into shallow and deep traps, (4) detrapping of the electrons and holes, and (5) recombination of electron–hole pairs as light emission. (b) The top part represents how nonperiodic disorder and defects in a semiconductor lattice create localization of the charge carriers inside the trap's energy well and the bottom part shows the newly introduced energetic levels and how traps slow down the transport of charge carriers through trapping and detrapping events. Source: Adapted from Jin et al. [28]. (c) The state density in a disordered semiconductor and the radiative (rad.) and nonradiative (nonrad.) recombination processes. Source: Reproduced with permission from Jin et al. [28]; © 2020, Royal Society of Chemistry. (d) Summary of various possible excitation paths using various pumping sources from low energy ultraviolet (UV), visible (Vi), and NIR light, to ionizing irradiation like X-rays, trapping detrapping mechanisms of charge carriers involving various shallow and deep electron/hole traps, quantum tunneling of charge carriers, up-conversion persistent luminescence, and energy transfer process involved in persistent luminescence. Source: Liang et al. [29]/Springer Nature.

PersL process, electrons are first excited from a ground state to an excited state by a charging source such as UV or visible light, or high-energy ionizing radiation like X-rays. The excited electrons are then further photo-ionized into the conduction band (CB) of host materials with the help of continued excitation energy. Since the electrons are free to move in the CB, they can be easily trapped by either shallow (close to CB) or deep (a bit far from CB) traps. Since these electron traps form localized electronic states at energy levels which are different from carrier transport bands, they will get trapped energetically whenever photo-generated free carriers fall into these localized states (Figure 1.3b, top). Since these trap states have different equilibrium nuclear configurations, there is an additional energy barrier between the delocalized carrier transport energy band (CB or valence band [VB]) and localized state (in a trap). The mobility of the charge carriers (electrons and holes) in the crystal system therefore restricted energetically (Figure 1.3b, bottom). Such energy barriers occur because the empty and occupied defect energy states have different equilibrium nuclear configurations [28]. An additional external activation energy with an energy of $k_B T \sim 26$ meV wherein k_B = Boltzmann constant and T = temperature at room temperature is required by these trapped carriers in order to escape the localized state and get back into the CB or free carrier transport level. Moreover, only those defect-related traps whose energy levels are positioned between CB and VB are suitable to trap charge carriers [28]. The trap depth is defined by the energy difference between transport states and defect levels (ΔE). Any defects whose energy level exists above CB or below VB edges cannot act as trap states. As shown in Figure 1.3c, traps having small energy difference to CB and VB edges ($\Delta E \leq k_B T$) are called as shallow trap states while those energetically positioned toward the middle of band gap ($\Delta E > k_B T$) are called deep trap states. The small energy difference of the shallow traps makes them involved in both trapping and detrapping processes of the free charges and restricts their efficient movement. In contrast, due to higher energy difference, a deep trap sometime hinders detrapping process and facilitates the nonradiative recombination pathways (Figure 1.3c). Therefore, an additional form of energy by means of optical, thermal, or mechanical source is required to release these trapped charge carriers. The room temperature thermal energy may release the shallowly trapped carriers slowly and help to get back into the CB followed by emission due to electron–hole recombination resulting persistent luminescence (Figure 1.3d).

Recently Liang et al. provided an excellent summary of various complex mechanisms (steps 1–19) involve in the PersL process of PLMs, starting from possible excitation paths, trapping–detrapping mechanisms involve in various shallow and deep traps (Figure 1.3d) [29]. The electrons from the activator can be pumped to a higher energy level (step 1) by using a variety of excitation sources. Although both UV and visible light sources are widely used as pumping sources for PLMs, UV excitation source with photon energy higher than the band gap of host materials generates strong PersL than visible light (step 12) in most of the cases. However, when PLMs are considered for application in biological field, especially for bioimaging, it is necessary to have good charging ability with high tissue penetrating deep-red or NIR lights sources in order to facilitate the required in-situ recharging. Lanthanide-based

photon up-conversion process can be used to design such NIR excitable PLMs with anti-Stokes emission. This can be achieved through the energy transfer (ET) processes between the sensitizers and activators. Two or more incident low-energy NIR photons are absorbed by the sensitizers followed by sequential populations of the higher excited states of the activator via an energy transfer as shown in steps 15 and 16. The activators then emit a high-energy photon in the UV–Vis region to charge PLMs (step 18). On the other hand, high-energy X-rays will produce abundant electron–hole pairs through the Auger effect and Compton scattering (step 19). The negligible scattering and higher penetration depth of X-rays make them an alternative excitation source for PLMs. Both electrons and holes coexist as the primary charge carriers in PLM host matrices. The photo excitation of an electron may create a hole either in the activator or in valance band, which can be subsequently captured and then released by hole traps through migration across the VB (steps 7, 8, and 14). All these charge carriers created by various sources of excitation energies are then subsequently captured by the shallow and deep traps (steps 2, 7, 13, and 14), followed by their gradual released back to the activators (steps 3 and 8) to trigger PersL (step 4). In many times, an ET process between two different types of emitters is an effective way to expand the spectrum of PLMs (steps 9–11). As mentioned before, shallowly trapped electrons can be transferred back to the activators easily via CB at room temperature to generate PersL; however, deeply trapped electrons find such escape difficult and need external stimuli like heating, light irradiation, and mechanical force (step 5). Because the shallow-trap-based discharge is fast and generates only short PersL while the deep-trap-based discharge is difficult and needs external stimuli, a quantum tunneling (QT) model has been proposed for the deeply trapped electrons, which showed the ultralong (tens of hours) PersL (step 6). Therefore, the depth of the traps plays the most crucial role in determining the performance of PLMs. Shallow trap states result in high intensity and short PersL due to quick electron–hole recombination, while deep traps result in low intense long PersL. Many times, deep traps hinder detrapping process due to higher energy difference and facilitates nonradiative recombination pathways, which causes less light yield. Hence, defect-related trap depth engineering plays a crucial role in designing efficient PLMs. Different types of crystal imperfections, such as vacancies, interstitial ions, impurities, and dopants, can act as electron traps with a broad energy distribution in depth.

After a brief discussion of PersL processes, we will now explain the PersL mechanisms by considering various proposed models, including the CB-VB model, the energy band model through CB and VB engineering, the self-electron/hole trapping–detrapping model, the QT model, the cation vacancy model, and the anion vacancy model, as discussed below.

1.2.1 CB-VB Model

The CB-VB model is based on hole and electron trapping–detrapping processes through VB and CB, respectively. This requires the energetic position of traps near VB or CB because the localization or trapping of the free charge carriers (holes

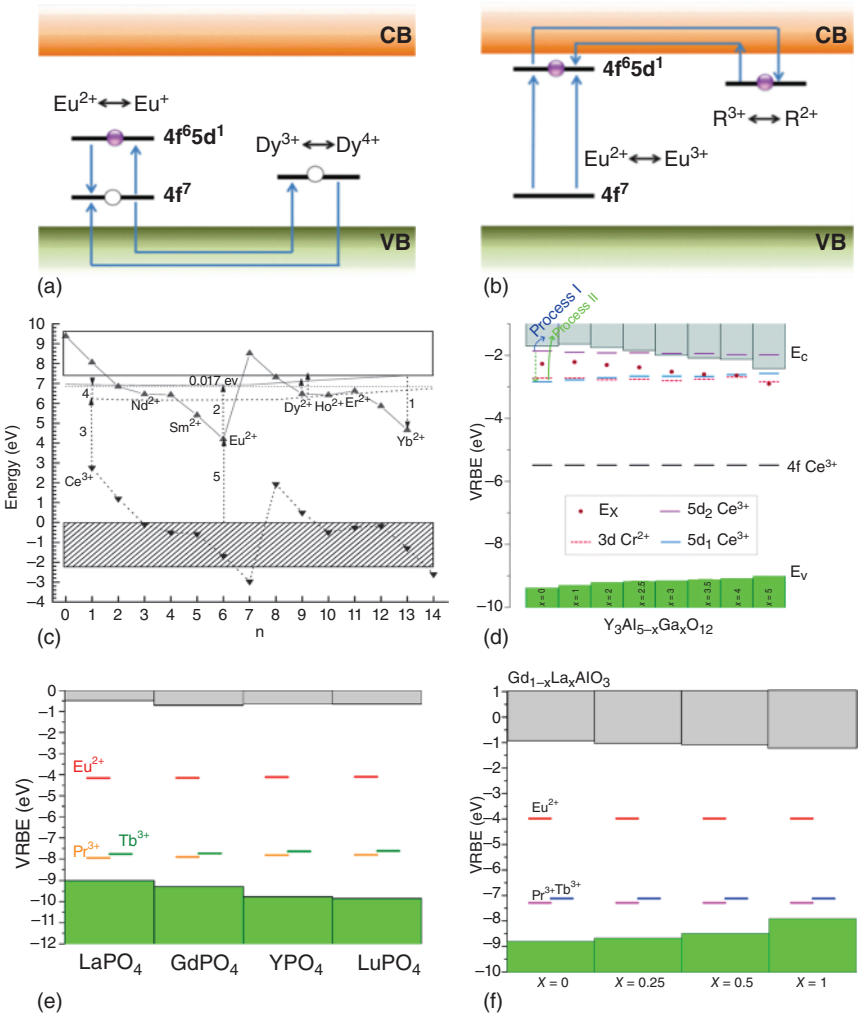

Figure 1.4 Various proposed PersL mechanisms: (a) Hole trapping–detrapping model through VB and CB. (b) Electron trapping–detrapping model through VB and CB. Source: Li et al. [18]/Royal Society of Chemistry. (c) Energy level scheme of $SrAl_2O_4$ host. Source: Dorenbos [30]/IOP Publishing. (d) Stacked VRBE diagrams of $Y_3Al_{5-x}Ga_xO_{12}$: Ce^{3+},Cr^{3+} (x = 0, 1, 2, 2.5, 3, 3.5, 4, and 5), Source: Ueda et al. [31]/Royal Society of Chemistry. (e) Stacked VRBE diagram of $REPO_4$ (RE = La, Gd, Y, and Lu) with the binding energy in the ground states of Eu^{2+}, Pr^{3+}, and Tb^{3+}. Source: Lyu and Dorenbos [32]/Royal Society of Chemistry. (f) Stacked VRBE diagram of $Gd_{1-x}La_xAlO_3$ (x = 0, 0.25, 0.5, and 1). Source: Luo et al. [33]/American Chemical Society.

and electrons) in the traps happens via VB and CB only. As discussed earlier, the detrapping process of shallow trap carriers is easier than that of the deep trap carriers; we shall discuss the hole and electron trapping–detrapping processes below by giving some specific examples.

Hole trapping–detrapping processes can be found in the case of $SrAl_2O_4$:Eu^{2+},Dy^{3+} as proposed by Yamamoto and Matsuzawa (Figure 1.4a) [34]. They considered holes

as the main charge carriers as supported by their photoconductivity measurements. When an Eu^{2+} ion is excited by a photon, a hole is possibly escaped from the ground state of Eu^{2+} ion to the VB and leaving behind an Eu^{+} ion. In the VB, the hole is free to move and subsequently captured by the Dy^{3+} ions, which has formed a shallow hole-trap near the VB and resulting in a Dy^{4+} ion. The room temperature thermal energy then releases the hole from Dy^{4+} ion into the VB and followed by recombination with the electron of Eu^{+} ion and generating Eu^{2+} again by releasing a photon.

Later, Tanabe et al. disagreed with this hole trapping–detrapping model because the reduction of Eu^{2+} to Eu^{+} and the oxidation of Dy^{3+} to Dy^{4+} requires huge amount of energy and possible only under ambient conditions. They propose a new model in which Eu^{3+} is created after leaving an electron to CB while the Dy^{3+} ion captures the escaped electron through CB and forms Dy^{2+} [35, 36]. This is known as electron trapping–detrapping model (Figure 1.4b), which is exactly a mirror image of the hole trapping–detrapping model. This mechanism was strongly supported by the existence of Eu^{3+} species under excitation through the X-ray Absorption Near Edge Spectroscopy (XANES) results [37], but the reduction of Dy valence state from 3+ to 2+ is still a debate and has not been confirmed experimentally by Electron Paramagnetic Resonance (EPR), X-ray photoelectron spectroscopy (XPS) or XANES techniques. Later, Holsa et al. also agreed that Eu^{+} species are unstable in aluminate. They proposed that codoping Re^{3+} ion like Dy^{3+} may create new defect-modulated trap centers due to the charge imbalance [38]. Moreover, they also observed a higher duration of PersL from $SrAl_2O_4$:Eu,Sm than $SrAl_2O_4$:Eu when Sm^{3+} ion is added. The argument that co-dopant ions like Dy^{3+} and Sm^{3+} are only modulating trap centers due to charge imbalance was supported by the fact that lower PersL duration was observed when Sm^{3+} ions are easily reduced to Sm^{2+} in the N_2–H_2 atmosphere. Recently, Wang et al. have demonstrated super-long PersL from $SrGa_2O_4$:Cu^{2+} [39]. Through a combined experimental and theoretical studies, they proposed that O vacancies and the −1 charged Ga vacancies create hole traps close to the VB. Herein, the excitation occurs through charge transfer transition from O^{-} to Cu^{2+} and leaves behind a hole in VB. The hole is then trapped by −1 charged Ga vacancies followed bydetrapping and recombination to give red PersL from $SrGa_2O_4$:Cu^{2+}.

1.2.2 Energy Band Model via CB and VB Engineering

It is always easier and in a more convincing way to explain electron and hole trapping–detrapping mechanisms if the absolute energy of VB, CB, excited and ground states of luminescence centers as well as trap states can be determined and presented in one energy level diagram. While there has been an ongoing debate for about 10 years on PersL mechanism behind $SrAl_2O_4$:Eu^{2+},Dy^{3+}, P. Dorenbos first constructed the famous energy level scheme of $SrAl_2O_4$ host with two zigzag curves of divalent and trivalent lanthanide ions in 2005 (Figure 1.3c) [30]. From the respective energy level position of various divalent lanthanides, it was proposed that trivalent lanthanide ions such as Nd^{3+}, Dy^{3+}, Ho^{3+}, and Er^{3+} can act as potential electron trapping centers in $SrAl_2O_4$:Eu^{2+},Ln^{3+} since the ground states of the Ln^{2+}

species are located below the bottom of CB (Figure 1.4c). On the other hand, since the trap depths of Eu^{2+} from VB is very high, Eu^{2+} can act as a stable hole trapping center and thereby act as emitting or electron–hole recombination center.

Thus, the electron trapping–detrapping mechanism involving the Eu^{2+}/Dy^{3+} and Eu^{3+}/Dy^{2+} redox couple, that is, excitation of 5d electron of the Eu^{2+} ion to the CB followed by trapping at Dy^{3+} trap, can be explained. Since Nd^{2+} ions have similar depth like Dy^{2+}, the same diagram can also explain the sensitization of Nd^{3+} when codoped with Eu^{2+} as reported in Matsuzawa's paper [10]. Therefore, with the help of such diagram shown in Figure 1.4c, it is now possible to predict a few critical things as follows: (i) the nature of the charging process, that is, electron and/or hole transfer, (ii) differentiation of the emission canters and trap centers of PersL and the role of co-dopants. From Figure 1.4c, it can be said that Eu^{2+} and Ce^{3+} usually act as emission centers because they prefer to be stable as hole traps due to large energy gap between the ground state and the top of VB. On the other hand, due to moderate or small trap depth with respect to CB, Nd^{3+}, Dy^{3+}, Ho^{3+}, and Er^{3+} can act as efficient electron trapping centers [4].

Such energy level scheme can also provide good guidance to control and alter PersL properties by controlling the trap depth or by altering the energy level of CB or VB edge in a controllable manner, known as CB engineering and VB engineering. For example, the PersL mechanism due to Ce^{3+} in $Y_3Al_{5-x}Ga_xO_{12}$:Ce^{3+},Cr^{3+} ($x = 0$–5) can be tuned by altering the trap depth by changing the energy gap between CB edge and the ground state of Cr^{2+}. As shown in Figure 1.4d, it is possible to construct the vacuum referred binding energy (VRBE) diagrams of $Y_3Al_5O_{12}$-$Y_3Ga_5O_{12}$ solid solutions wherein the energy level of 4f and $5d^{1,2}$ states of Ce^{3+} as well as 3d ground state of Cr^{2+} are shown, and by substituting Ga^{3+} at the tetrahedral and/or octahedral sites, a systematic variation of trap depth can be realized as strongly supported by the thermoluminescence (TL) study [31].

Similarly, when La, Gd, Y, and Lu orthophosphates were doped with different lanthanide ions, their VRBE diagrams can be constructed as shown in Figure 1.4e [32]. From the TL 2D mapping of Eu^{3+} and Tb^{3+} codoped YPO_4 after ceasing excitation, it was observed that only TL emission due to $^5D_0 \rightarrow {}^7F_J$ ($J = 1, 2, 3$, and 4) transitions of Eu^{3+} were present while 4f-4f transitions of Tb^{3+} were totally absent. This confirmed that Eu^{3+} act as electron trapping and recombination centers while Tb^{3+} act as hole trapping centers. This experimental result can be clearly explained by considering the trap depths from the VRBE diagram. It was also explained that when Y^{3+} ions were substituted by isovalent La^{3+}, Gd^{3+}, or Lu^{3+} ions, the top of VB was altered in a controllable way. This is known as VB engineering to tune the trap depths of hole trapping centers. Likewise, the VRBE diagram of Gd_{1-x} La_xAlO_3 ($x = 0$, 0.25, 0.5, and 1) in Figure 1.4f showed how the trap depth can be altered by doping La at Gd position [33].

1.2.3 Self-Electron/Hole Trapping–Detrapping Model

The examples described above indicate that it is feasible to tailor the trap depth (ΔE) of electron or hole traps by CB or VB engineering and subsequently controlling the

recombination process and PersL characteristics of PLMs with prior knowledge of various energy levels of lanthanide ions within the bandgaps of certain matrices. However, these CB-VB engineering models are based on the energy level position of dopants and co-dopants, which act as trap centers inside the band gaps of PLM hosts. Also, it is difficult to explain the intense PersL in some single activator-doped PLMs by Cr^{3+} or Mn^{2+} [40]. Although there are many explanations that intrinsic and lattice defects may act as electron or hole traps, in many cases, it is possible that the activation center itself is serving as both emission and trap centers, which leads to the self-electron/hole trapping–detrapping model. This happens only when activators have multi-valence states with a self-redox nature in particular host matrices. For example, the VRBE diagrams of Cr-doped $LaAlO_3$ can be constructed by putting absolute energy levels of Cr^{3+} and Cr^{2+} (Figure 1.5a) [41]. The VRBE diagram indicates that Cr^{3+} ion may act as a deep hole trapping or a recombination center due to the large trap depth (~1.5 eV) from the top of the VB, while it may also act as an intermediate or shallow electron trapping canter due to relatively lower trap depth (~1.3 eV) of Cr^{2+} from the bottom of the CB. A similar explanation can also be given

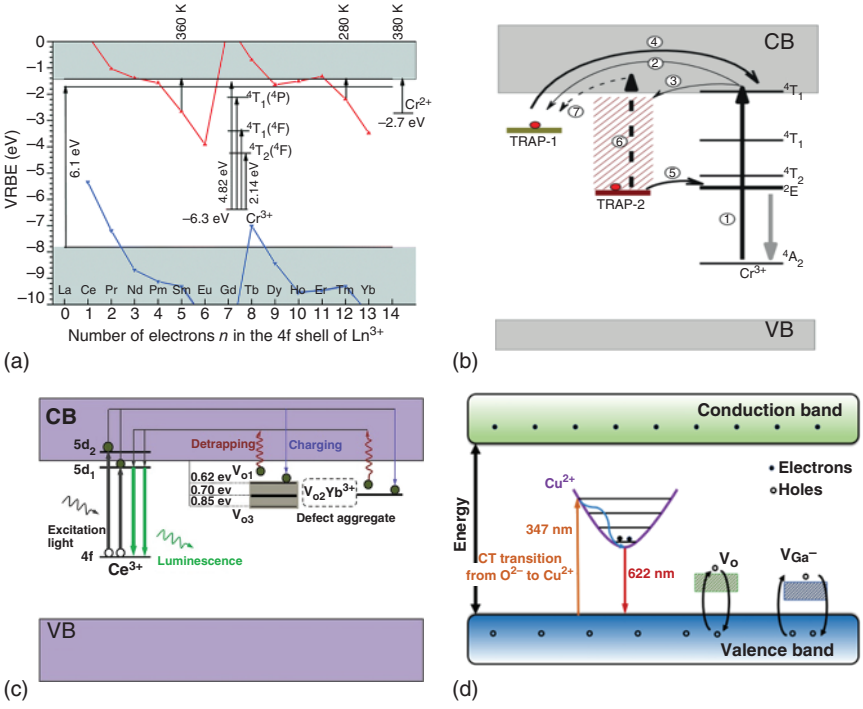

Figure 1.5 (a) The VRBE diagram with self-electron and hole trapping–detrapping model in chromium-doped $LaAlO_3$. Source: Adapted from Katayama et al. [41]. (b) QT model of NIR PersL in Cr^{3+}-doped $LiGa_5O_8$. Source: Adapted from Liu et al. [42]. (c) Oxygen vacancy as electron traps for the PersL mechanism of YAGG:Ce^{3+},Yb^{3+}. Source: Yang et al. [43]/American Chemical Society. (d) Oxygen and Ga vacancy as hole trap for the PersL mechanism of $SrGa_2O_4$:Cu^{2+}. Source: Wang et al. [39]/American Chemical Society.

in other matrices such as $GdAlO_3$, $YAlO_3$, and $LuAlO_3$ due to similar ground state locations of Cr^{2+} and Cr^{3+} in their VRBE diagrams.

1.2.4 QT Model

While most of the above-mentioned CB-VB models explained the charge trapping in shallow trap states, QT model explains super-long PersL involving deep traps with higher trap-depth energy. The words of quantum tunneling describe a quantum mechanical phenomenon when particles tunnel through a barrier, which is not possible classically. In a few cases of deep traps, it is possible that room temperature is not sufficient to release charge carriers from traps, but tunneling of electrons or holes might occur between deep trap states and near energy state levels of activators. For example, Cr^{3+}-doped zinc gallogermanate showed super-long PersL in 650–1000 nm region and lasted for 15 days (360 hours) [44]. Similarly, Cr^{3+}-doped $LiGa_5O_8$ showed NIR PersL, which lasted more than 1000 hours [42]. When charged by UV light, these PLMs showed a strong afterglow suggesting that the approximate energy required for ionizing Cr^{3+} activator in $Zn_3Ga_2Ge_2O_{10}$ or $LiGa_5O_8$ host is near to the CB. However, these same PLMs were also found to give weak but super long PersL when charged by low-energy visible light (400–630 nm). This interesting phenomenon can be explained based on QT process as shown in Figure 1.5b. When charged by visible light, electrons from the ground state of Cr^{3+} ions may be promoted to higher energy levels, which are close to deep traps below ionization threshold. Subsequently, the deep traps get filled through the tunneling process from the closest energy levels of Cr^{3+} ions. This explains the charging of deep traps by low energy light while the reverse tunneling recombination procedure explain the super long afterglow as it is difficult to release the carriers into CB or VB directly due to high energy barrier.

1.2.5 Cation and Anion Vacancy Model

Most of the examples given above involve various lanthanide or transition metal ions as traps, either when being used as co-dopants or acting as self-trap centers in some cases. However, there are also many examples in which intrinsic defects, such as cationic or anionic vacancies, act as hole or electron trap centers. Especially, in oxide-based PLMs, oxygen vacancy is often found to act as electron traps. For instance, Clabau et al. suggested that oxygen vacancies can act as efficient electron traps in $SrAl_2O_4$:Eu^{2+},Dy^{3+} [45]. Therefore, even if codopant ions such as Dy^{3+} act as efficient traps for Eu^{2+} doped PLM matrices as explained by the CB-VB energy diagram, it is very much feasible that oxygen vacancies also form different types of shallow or deep traps. Furthermore, these models could be constructed based on the identification and characterization of vacancies by many sophisticated techniques, such as XPS, EPR, and positron annihilation lifetime spectroscopy (PALS). For example, oxygen vacancies were found to be responsible for enhancing the PersL of $Y_3Al_2Ga_3O_{12}$:Ce^{3+},Yb^{3+} significantly when this PLM was heated in 10% H_2/90% Ar atmospheres [43]. In addition to Yb^{3+}, oxygen vacancies also act as efficient

electron trap canters as shown in Figure 1.5c. In this case, the existence of oxygen vacancies in the $Y_3Al_2Ga_3O_{12}:Ce^{3+},Yb^{3+}$ PLM was characterized by XPS and EPR measurements. Similarly, both neutral oxygen vacancy and negatively charged Ga vacancies were found to act as hole-trap in $SrGa_2O_4:Cu^{2+}$ and generate super-long red PersL (Figure 1.5d) [39]. Therefore, depending on its charge, oxygen vacancies can act both as electron and hole trap centers while the negatively charged cationic vacancies act as hole trap centers.

1.3 Types of PLMs

1.3.1 Inorganic PLMs

Figure 1.6a represents a typical PersL material comprises three components: host (H), luminescent emitter (E), and trapping centers (T). IPLMs can be categorized into ultraviolet (UV), visible, and near-infrared (NIR) light-emitting PLMs according to the emitter's specific emission range. Figure 1.6b,c shows various UV and visible light emitters, respectively. In many cases, some emitters have shown PersL both in the UV and visible wavelength regions.

In Figure 1.7, we present a few examples of PersL spectra along with the decay profiles of these UV, visible, and NIR PLMs. The applications of PLMs are mostly dependent on their emission wavelengths; hence, some PLMs are more suitable for specific applications than others. For instance, PLMs having visible PersL are useful as luminous signage and lighting sources when it is desired to have high visibility in the dark. For biomedical applications, NIR PLMs are the most desirable candidates due to the high tissue penetrability of NIR light [17, 18]. On the other hand, UV PLMs find applications in persistent disinfection, "solar-blind" tagging, persistent photocatalysis, and "device-free" phototherapy [46]. Below we have summarized many representative UV, visible, and NIR PLMs.

1.3.1.1 UV PLMs

While most efforts have been devoted to design and develop efficient visible and NIR PLMs along with critically understanding of their PersL mechanism in the last three decades, UV PLMs have started to receive attention from the research community only in the last decade. Except for a few Pb^{2+} or Ce^{3+} doped UVA PLMs reported in 2002 and 2003, major interest in developing UV PLMs was aroused only after 2015 [48, 53–55]. The challenges in finding emitters with high emissive energy levels and suitable host matrices with large band gaps, along with having efficient charge traps located at high energy positions, are the main reasons for the limited number of reported UV PLMs. However, since the demand for UV light emitting devices for disinfection technology has grown significantly during the COVID-19 pandemic [56], researchers are giving significant effort to design and develop various UV PLMs as reflected by their increasing number of reports [46]. Depending on the emission wavelengths, UV PLMs can be further classified into UVC (200–280 nm), UVB (280–315 nm), and UVA (315–400 nm) PLMs. Due to

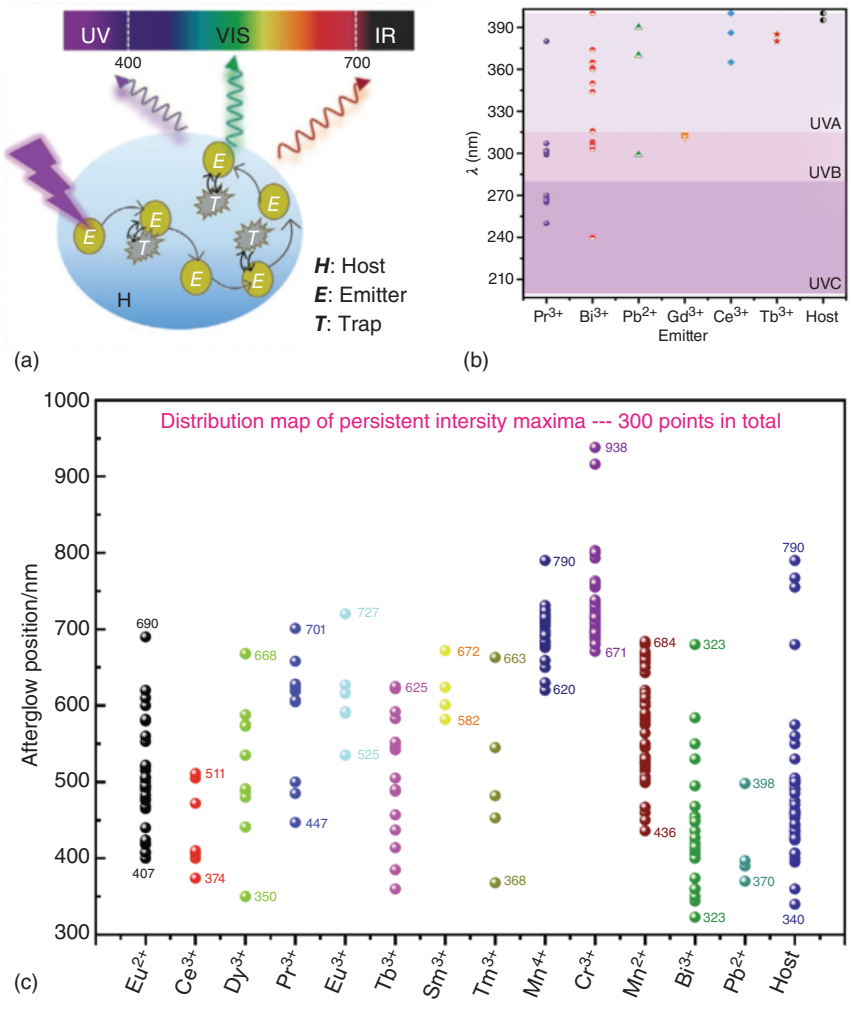

Figure 1.6 (a) Schematic representation of a PersL material comprising a host (H), an emitter (E), and traps (T). The PersL material emits possibly in UV, Vis, or IR range upon UV irradiation. Source: Adapted from Wang and Mao [46]. (b) Examples of various UV PersL emitters, such as Pr^{3+}, Bi^{3+}, Pb^{2+}, Gd^{3+}, Ce^{3+}, Tb^{3+}, and wide-band compounds, and their emitting wavelengths distributed in UVA, UVB, and UVC regions. Source: Adapted from Wang and Mao [46]. (c) Example of various visible light PersL emitters, such as $Eu^{2+/3+}$, Ce^{3+}, Dy^{3+}, Sm^{3+}, Tm^{3+}, Tb^{3+}, Pr^{3+}, Mn^{2+}, Mn^{4+}, Cr^{3+}, Bi^{3+}, Pb^{2+}, and wide-band compounds, and their emitting wavelengths distributed in UVA, blue, green, yellow, red and NIR regions. Source: Adapted from Kang et al. [47].

numerous unique applications of functional materials within each range of these UV wavelengths, UV PLMs show unparalleled potentials over visible and NIR PLMs. So far, UV PLMs can be developed by doping activators such as Pr^{3+} ($4f^2$), Gd^{3+} ($4f^7$), Ce^{3+} ($4f^1$), Bi^{3+} ($6s^2$), or Pb^{2+} ($6s^2$) into suitable host matrices. Among them, Pr^{3+} and Bi^{3+} activators can generate PersL in the UVA, UVB, and UVC

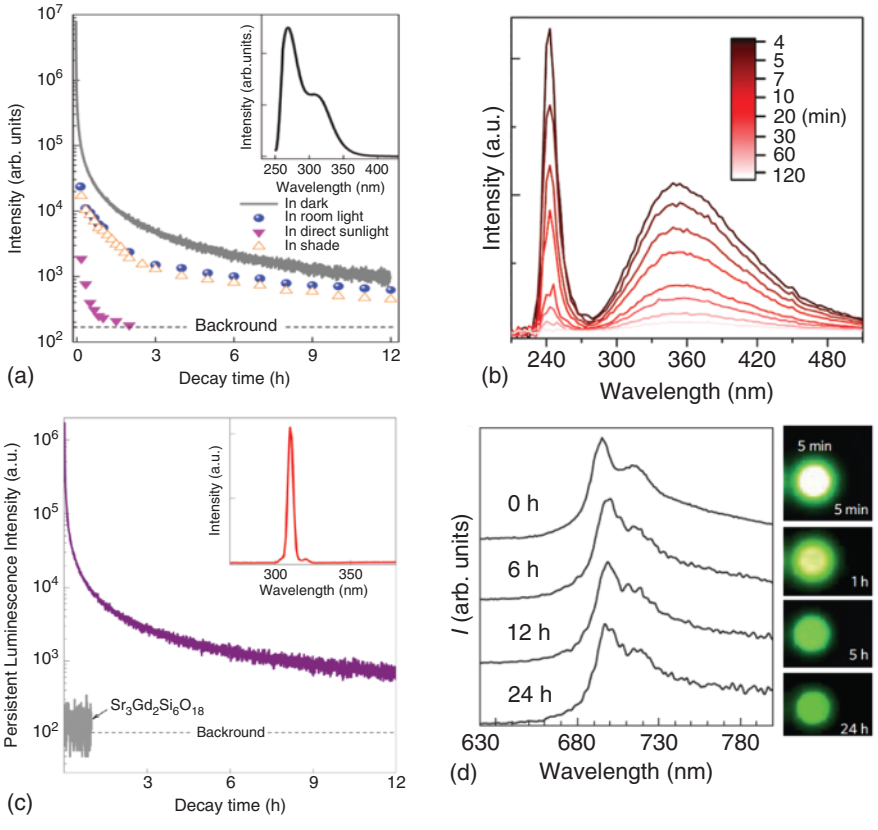

Figure 1.7 Representative PLMs of Pr^{3+}, Bi^{3+}, Gd^{3+}, Ce^{3+}, Mn^{2+}, and Cr^{3+}-doped compounds. (a) PersL decay curves of $Ca_2Al_2SiO_7$:Pr^{3+} at 268 nm in different light environments, including in the dark, under room light, in direct sunlight, and in the shade after charged by 254 nm UV light along with its emission spectrum as shown in the inset. Source: Wang et al. [48]/Springer Nature/CC BY 4.0. (b) PersL emission spectra of YPO_4:Bi^{3+} recorded at different delayed times including 4, 5, 7, 10, 20, 30, 60, and 120 minutes after ceasing X-ray irradiation. Source: Liu et al. [49]/John Wiley & Sons. (c) PersL decay curves of $Sr_3Gd_2Si_6O_{18}$:Pr^{3+} peaking and $Sr_3Gd_2Si_6O_{18}$ at 311 nm upon 254 nm charging along with the PersL spectrum of $Sr_3Gd_2Si_6O_{18}$:Pr^{3+} shown in the inset. Source: Wang et al. [50]/Royal Society of Chemistry. (d) PersL intensity of $Zn_3Ga_2Ge_2O_{10}$:0.5%Cr^{3+} monitored at 713 nm as a function of time after charged by UV light at 254 nm. The right-hand side of the picture shows the photograph of NIR PersL of the same compounds at various time interval after ceasing the excitation source. Source: Pan et al. [44]/Springer Nature. (e) PersL emission spectra of Li_2ZnGeO_4:$t$$Mn^{2+}$ (t = 0, 0.0025, 0.005, 0.01, 0.015, and 0.02) visible PLMs after removing excitation source at 254 nm. Insets: the photos of Li_2ZnGeO_4 and Li_2ZnGeO_4:Mn^{2+} samples under sunlight, under the irradiation by 254 nm of excitation wavelength and at different time intervals after ceasing the excitation source. Source: Adapted from Jin et al. [51]. (f) Photographs of PL (top; under UV light illumination) and PersL (bottom; 10 seconds after excitation ceased) from $YSiO_2N$:Ce^{3+} and $YSiO_2N$:Ce^{3+},Ln^{3+} (Ln = Sm, Tm) samples. Source: Adapted from Kitagawa et al. [52].

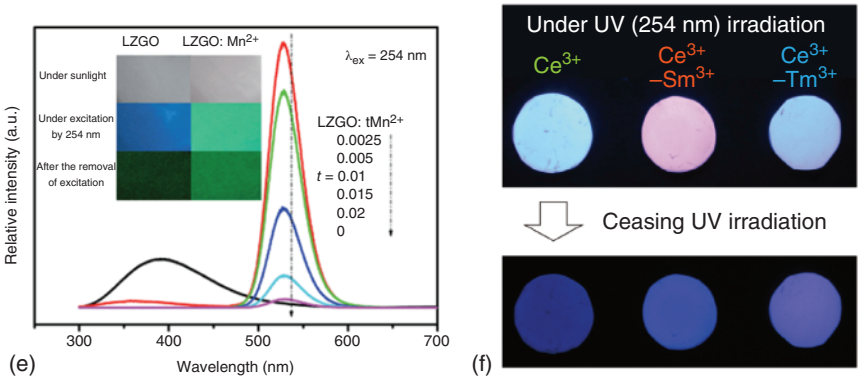

Figure 1.7 (*Continued*)

regions, Pb^{2+} can yield UVA and UVB PersL, Gd^{3+} may produce UVB PersL, and Ce^{3+} and some undoped wide-band compounds might create UVA PersL [46].

Generally, host crystals and charging wavelength determine whether the PersL emitted from these activators fall at UVA, UVB, or UVC region. For example, Pr^{3+} activator generates UVA, UVB, or UVC PersL due to its high-energy and lattice-sensitive 4f5d state [54]. It can be excited by UV irradiation through the parity-allowed electric-dipole $4f^2 \rightarrow 4f5d$ transition. When there are suitable trap centers in host matrices, the excited Pr^{3+} can return from the lowest excited 4f5d state to the $4f^2$ ground and give UV PersL. The first UVC PLM was reported by Yang et al. from Pr^{3+} doped Cs_2NaYF_6 with lasted PersL for two hours when charged by the X-rays in 2018 [55]. Fluoride vacancies acted as an effective trap for the large number of electrons triggered due to X-ray irradiation. Later, Pan et al. developed a UVC PLM by doping Pr^{3+} into melilite $Ca_2Al_2SiO_7$, which showed a broadband UVC PersL emission at 268 nm lasting for >12 hours when charged with 254 nm UV lamps [48]. $Lu_3Al_2Ga_3O_{12}$,Pr^{3+} showed UVB PersL lasting for several hours [57], while Pr^{3+}-doped $(Ca_{1.5}\ Y_{1.5})(Al_{3.5}\ Si_{1.5})O_{12}$ showed dual ultraviolet C (UVC) and ultraviolet B (UVB) PersL due to the existence of two different Pr^{3+} environments at Ca^{2+} and Y^{3+} sites [58]. Both UVC and UVB PersL lasted over 12 hours [57, 58].

The ground state of Bi^{3+} ion is $^1S_0$ ($6s^2$ configuration) while its excited levels are composed of three triplet states, that is, $^3P_0$, $^3P_1$, and $^3P_2$, and a singlet state $^1P_1$ in a sequence of increasing energy (6s6p configuration). When excited with UV light, the $^1S_0 \rightarrow {}^3P_0$ transition is strictly forbidden; however, due to the spin–orbit coupling and coupling to asymmetrical phonon modes, the $^1S_0 \rightarrow {}^3P_1$ and $^1S_0 \rightarrow {}^3P_2$ transitions become partially allowed. On the other hand, the $^1S_0 \rightarrow {}^1P_1$ transition is an allowed electric dipole transition, hence, Bi^{3+} shows emission typically from the $^3P_1$ excited states to the $^1S_0$ state. Bi^{3+}-doped PLMs show PersL mostly in the UVA and UVB regions or in the UVC region in some cases. For example, Liu et al. reported both UVC (maximum at 240 nm) and UVA PersL from Bi^{3+} doped YPO_4 after ceasing X-ray irradiation source [49]. The UVC and UVA are attributed to $^1S_0 \rightarrow {}^3P_1$ emission transition of Bi^{3+} and that of Bi^{3+} pairs, respectively. Various traps such as Y vacancies, Y-O vacancy complexes, and Bi^{3+} itself in some cases at suitable energy

depths are responsible for the PersL. Bi^{3+} activator has also showed UVA and UVB emissions in other matrices such as $LiScGeO_4$ (~361 nm UVA emission and lasting >12 hours) [59], $Y_3Ga_5O_{12}$ (~316 nm UVA emission and lasting >30 minutes) [60].

Pb^{2+} has an electronic configuration similar to Bi^{3+}, that is, $[Xe]4f^{14}5d^{10}6s^2$. It shows emissions due to transition from $^3P_0$, $^3P_1$, $^3P_2$, and $^1P_1$ excited states to $^1S_0$ ground state in the ground state configuration of $6s^2$ and generates emission in UV or blue region. For example, $Sr_2MgGe_2O_7$:Pb^{2+} showed a broadband UVA PersL emission at ~370 nm and lasted for more than 12 hours when charged by 254 nm light [54]. $Sr_3Y_2Si_6O_{18}$:Pb^{2+} showed UVB PersL emission at ~299 nm and lasted for similar hours of duration when charged with the same UV light [50]. However, compared to Bi^{3+} doped PLMs, Pb^{2+} doped PLMs have limited reports and have not been explored widely, which might be due to the toxicity of Pb^{2+}.

Ce^{3+} is another emitter in the UV and visible spectral regions. It has an allowed-parity 4f–5d transitions in different ionic crystals. $Y_3Al_5O_{12}$:Ce^{3+} is widely used commercial yellow-green phosphor for fabrication of white-light LEDs. However, due to the lattice-sensitivity of 4f–5d transitions of Ce^{3+}, the emission in the UV region of Ce^{3+}-based PLMs is dependent on host matrices. For example, Ce^{3+} doped $Sr_2Al_{1.7}B_{0.3}SiO_7$ showed PersL at ~400 nm and lasted for several minutes, but Ce^{3+} doped CaB_2O_4 showed PersL ~365 nm and lasted for several hours [61, 62]. UVA and near-UV PersL emissions are useful for photocatalytic applications in dark conditions. Apart from UVA PLMs, many UVB or UVC PLMs based on Ce^{3+} have also been reported.

Gd^{3+} has a stable $4f^7$ configuration and its excited states are all above 30 000 cm^{-1}, in comparison to other luminescent ions. Its f–f transitions within the $4f^7$ configuration are forbidden. Furthermore, it has no tendency to be oxidized or reduced in a phosphor, which makes its electron transfer to trapping states difficult. This is why it is hard to get direct PersL from Gd^{3+} ion itself. However, when Pr^{3+}, Bi^{3+}, or Pb^{2+} ions are codoped with Gd^{3+} as PersL sensitizers, Gd^{3+} ions give PersL through a persistent energy transfer process. For example, $Sr_3Gd_2Si_6O_{18}$:Pr^{3+} showed narrow band UVB PersL at ~311 nm and lasted for >12 hours when charged with a 254 nm UV lamp. The narrow band UVB PersL generated due to energy transfer from the sensitizer Pr^{3+} to emitter Gd^{3+}, which emits narrow band UV light at ~311 nm due to $^6P_{7/2} \rightarrow {}^8S_{7/2}$ transition [50]. Similarly, Bi^{3+} ion is another efficient sensitizer while developing Gd^{3+}-based PLMs due to the overlapping of the $^3P_1 \rightarrow {}^1S_0$ broadband emission of Bi^{3+} (~303 nm) and $^8S_{7/2} \rightarrow {}^6P_J$ absorption band of Gd^{3+} ions [63]. Pb^{2+} ions can also be used as an alternate sensitizer because of their absorption and emission bands in the suitable UV spectral region. Following this persistent energy transfer process, many other Gd^{3+} containing PLMs codoped with Pr^{3+}, Bi^{3+}, or Pb^{2+} have been rapidly developed [50].

1.3.1.2 Visible PLMs

As mentioned earlier and suggested by hundreds of reports available today, visible PLMs have received more investigation efforts since the invention of $SrAl_2O_4$:Eu^{2+},Dy^{3+} compared to UV and NIR PLMs. Therefore, it is difficult for us to provide a catalog of all the existing visible PLMs in this chapter. Rather

we discussed the best-known PLMs in each segment of the visible region by categorizing visible PLMs into blue (400–490 nm), green (490–590 nm), yellow (540–610 nm) and red (590–680 nm) PLMs. As mentioned earlier, ZnS:Cu,Co was the dominant green PLM used for both military and civil purposes until the twentieth century. Later, the first new generation of green PLM $SrAl_2O_4:Eu^{2+}/Dy^{3+}$ was developed in 1996, which shows bright green PersL at ~520 nm and lasted for over 30 hours [10]. The codopant Dy^{3+} ion helps to achieve a far higher initial PersL intensity and a much longer lifetime compared to the commercially used ZnS:Cu,Co. Other famous strong green PLMs include $Ba_2MgSi_2O_7:Eu^{2+},Tm^{3+}$ and $Ca_2MgSi_2O_7:Eu^{2+},Dy^{3+}$ [64, 65]. Other than Eu^{2+} ions, activators such as Tb^{3+}, Ce^{3+}, and Mn^{2+} were also explored to generate green PersL when doped in various matrices. For example, $CaZnGe_2O_6:Tb^{3+}$ showed green emission lasting more than four hours while $Li_2ZnGeO_4:Mn^{2+}$ and $Zn_2GeO_4:Mn^{2+}$ showed green PersL peaking around 528–530 nm for several hours [51, 66, 67].

Since the excited state in the $4f^6 5d^1$ electron configuration of Eu^{2+} ion is dependent on crystal filed, its emission color in the solid state can be varied over a wide range of colors. The most widely commercially used blue PLM is $CaAl_2O_4:Eu^{2+},Dy^{3+}$ [68]. Other examples of Eu^{2+} based blue PLMs include $Sr_4Al_{14}O_{25}:Eu^{2+},Dy^{3+}$ [69], $Sr_2MgSi_2O_7:Eu^{2+},Dy^{3+}$ [70], and $Sr_3MgSi_2O_8:Eu^{2+},Dy^{3+}$ [71]. Ce^{3+} is another activator for blue phosphorescence when doped in proper hosts. It has additional advantage as it is less expensive than Eu^{2+}. The strong crystal field dependence of its 5d–4f transition makes it capable of producing a variety of colors. Examples of various Ce^{3+} doped blue PLMs with long persistent times >3 hours under UV light excitation include host matrices of Lu_2SiO_5 [72], $Ca_2Al_2SiO_7$ [73], and $SrAl_2O_4$ [74]. Apart from Eu^{2+} and Ce^{3+} activators, Tm^{3+} is another one that showed blue PersL when doped in $Zn_2P_2O_7$ [75]. The blue PersL is originated from the $^1D_2 \rightarrow {}^3H_6$, $^1D_2 \rightarrow {}^3H_4$, and $^1G_4 \rightarrow {}^3H_6$ transitions of Tm^{3+} and lasts for more than one hour.

Ce^{3+} and Eu^{2+} ions are also the main activators of developed yellow PLMs. For example, $Ca_2BO_3Cl:Eu^{2+},Dy^{3+}$ showed strong yellow PersL around 580 nm and lasted for 48 hours [76]. $Gd_3Al_2Ga_3O_{12}:Ce^{3+},Cr^{3+}$ showed yellow PersL around 540 nm when being excited with blue light [77]. Since the d-d transition of Mn^{2+} is also dependent on crystal filed, Mn^{2+} doped phosphors also show yellow PersL in addition to green afterglow, for example, $Cd_2Ge_7O_{16}:Mn^{2+}$ shows PersL at ~585 nm and lasted for three hours [78].

In the case of red PLMs, Eu^{3+} doped PLMs are found to be the most efficient ones owing to the abundant transitions from the excited $^5D_0$ level to the ^7F_J ($J = 0, 1, 2, 3, 4$) levels of its $^4f_6$ configuration. Examples include various oxysulfides, such as $Gd_2O_2S:Eu^{3+}$, $Gd_2O_2S:Eu^{3+},Si^{4+},Ti^{4+}$, $Gd_2O_2S:Eu^{3+},Mg^{2+},Ti^{4+}$, $Y_2O_2S:Eu^{3+},M^{2+},Ti^{4+}$ (M = Mg, Ca, Sr, and Ba), and $Y_2O_2S:Eu^{3+},Zn^{2+},Ti^{4+}$ [79–82]. Eu^{3+} acts as red emission centers in both Y_2O_2S and Gd_2O_2S hosts, while Mg^{2+} and Ti^{4+} replace the lattice sites of Y^{3+} or Gd^{3+} ions to form traps that store energy transferred from the excited states and then gradually transfer it back to Eu^{3+}. Pr^{3+} is another rare earth ion that gives red PersL due to its $^1D_2 \rightarrow {}^3H_4$, $^3P_0 \rightarrow {}^3H_6$, and $^3P_0 \rightarrow {}^3F_2$ transitions when it was doped in perovskite-type oxides such as $SrZrO_3$, $CaTiO_3$, $NaNbO_3$ [83–85]. Apart from rare-earth activators, transition metal ions

such as Mn^{2+} can also give red PersL emission when being placed at octahedral sites. Red emission from octahedral coordinated Mn^{2+} ions originates from its parity-forbidden 3d–3d intra-atomic $^4T_1$ (^4G) → $^6A_1$ (6S) transition, while the same transition gives green emission when Mn^{2+} ions are tetrahedrally coordinated. One interesting example is that β-$Zn_3(PO_4)_2$:Mn^{2+},Ga^{3+} and γ-$Zn_3(PO_4)_2$:Mn^{2+},Ga^{3+} have different PersL spectra, i.e., the former shows long-lasting red PersL while the latter gives both green and red PersL [86]. This is because γ-$Zn_3(PO_4)_2$ has both 4 and 6-coordinated Zn^{2+} lattice sites available for Mn^{2+} ions, while β-$Zn_3(PO_4)_2$ only has 6-coordinated Zn^{2+} lattice sites to Mn^{2+} doping. On the other hand, Sm^{3+} ion is famous for generating reddish-orange light among the rare earth ions due to its $^4G_{5/2} \rightarrow {}^6H_J$ ($J = 5/2$, 7/2, and 9/2) transitions. For example, $Sr_3Sn_2O_7$:Sm^{3+} shows an intense reddish-orange PersL, which is clearly visible by naked eye in the dark and lasts for more than one hour after ultraviolet irradiation for five minutes [87].

1.3.1.3 NIR PLMs

Compared to the large number of reported visible PLMs, the number of NIR PLMs emitting in the spectral range of 700–2500 nm is still small. In the last few years, NIR PLMs have got intensive attention from the PersL community across the world due to the growing need to improve current optical imaging techniques. Consequently, several reviews have been published recently on various NIR PLMs with their specific applications, such as NIR bio-imaging, chemotherapy, photothermal therapy, etc. [88].

This is because NIR light has high transmittance through biological tissues and NIR phosphors constitute a radioactive-free imaging technique. Hence, developing efficient and novel NIR PLMs has become an emerging area of research interest. NIR PLMs can be classified according to their different PersL wavelengths into NIR-I and NIR-II/III PLMs with emissions in the 700–1100 and 1100–2500 nm regions, respectively. Both rare earth ions including Eu^{2+}, Eu^{3+}, Tb^{3+}, Nd^{3+}, Er^{3+}, Pr^{3+}, Ho^{3+}, Sm^{3+}, Tm^{3+}, Yb^{3+}, and Dy^{3+} and transition metal ions including Cr^{3+}, Mn^{4+}, Mn^{2+}, Ni^{2+}, and Co^{2+} have been used as activators for NIR PersL. In another way, activators including Cr^{3+}, Mn^{4+}, Mn^{2+}, Eu^{3+}, Eu^{2+}, Yb^{3+}, Pr^{3+}, Ce^{3+}, and Tb^{3+} are important for developing NIR-I PLMs, while those of Yb^{3+}, Pr^{3+}, Nd^{3+}, Co^{2+}, and Ni^{2+} have made great contributions toward the development of NIR-II/III PLMs. For example, Jia et al. first developed $La_3Ga_5GeO_{14}$:Cr^{3+} NIR-I PLM, which shows super-broadband emission in the 700–1100 nm region [89]. Later, Pan et al. developed a series of Cr^{3+} doped $Zn_3Ga_2Ge_2O_{10}$ NIR PLMs, which show super-long afterglow emission lasting for about 360 hours in the region of 650–1000 nm [44]. These PLMs can be activated after being exposed to sunlight for only one minute. Hence, they are useful not only for bio-imaging but also for night-vision surveillance and solar energy in outdoor environments. Kamimura et al. observed NIR-II afterglow in the region of 850–1400 nm from Sr_2SnO_4:Nd^{3+} phosphor [90]. NIR PLMs have also been developed by inducing energy transfer between ions like Cr^{3+} and Er^{3+} in $LaAlO_3$ perovskite [91]. When Er^{3+}, Cr^{3+}, and Sm^{3+} are co-doped into $LaAlO_3$, long NIR-I and NIR-III PersL can be observed at 734 and 1553 nm due to the ^2E (2G) → $^4A_2$ (4F) transition of Cr^{3+} and the $^4I_{13/2} \rightarrow {}^4I_{15/2}$ transition of Er^{3+},

respectively. The NIR-III PersL is generated due to energy transfer from Cr^{3+} to Er^{3+} while Sm^{3+} acted as traps. Ni^{2+} doped $Zn_3Ga_2Ge_2O_{10}$ also shows single-band PersL in the range of 1000–1600 nm for several hours [92].

1.3.2 Molecular PLMs

Compared to IPLMs with numerous examples available in the literature, work on MPLMs was started later. The number of MPLMs with PersL emission across all three wavelength regions as classified for IPLMs above is limited, especially in the UV region. While there are various possible PersL mechanisms involved in IPLMs as we discussed in the prior section, PersL of MPLMs is originated from two different processes involved, that is, RTP and TADF, which we have provided various examples accordingly below.

Luminescence from organic compound involves either singlet or triplet excited states, which results in fluorescence or phosphorescence, respectively (Figure 1.8a,b). When excited states and ground states have the same spin multiplicity (without spin changes), transitions involving these states are allowed as fluorescence. On the other hand, electrons are forbidden to jump between two states with different spin multiplicities, that is, intersystem crossing with spin changes, which gives phosphorescence [15]. For most cases, the ground states of organic compounds are singlets (S_0 state), so the transition of excitons from

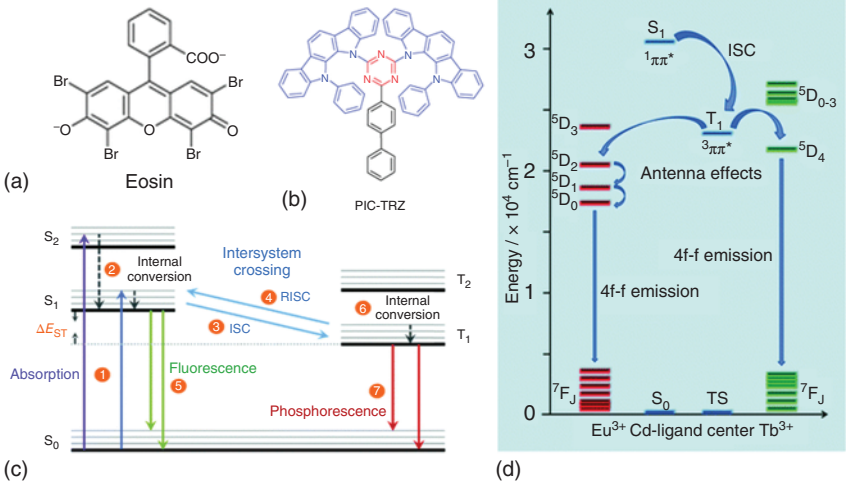

Figure 1.8 (a,b) Two typical TADF molecules. (c) Jablonski diagrams of fluorescence (1 → 2 → 5), phosphorescence (1 → 2 → 3 → 6 → 7), and thermally active delayed fluorescence (1 → 2 → 3 → 4 → 5) from organic molecules where 1: absorption, 2 and 6: internal conversion, 3: intersystem crossing (ISC), 4: reversible intersystem crossing (RISC), 5: fluorescence, 7: phosphorescence. Source: Yang et al. [15]/Royal Society of Chemistry. (d) Schematic energy level diagram and the energy transfer process in Cd–Eu/Tb-CP systems. Source: Yang et al. [93]/Royal Society of Chemistry.

the lowest singlet excited state to the ground state, that is, $S_1 \rightarrow S_0$ transition, leads theoretically allowed fluorescence, which is a fast process occurring with a lifetime of nanoseconds. On the contrary, phosphorescence occurs with a much longer lifetime ranging from microseconds to milliseconds due to the theoretically forbidden transition of excitation from T_1 state to S_0 ground state. Furthermore, transitions between excited states with different spin multiplicities such as S_1 and T_1 are also theoretically forbidden. When the energy gap (ΔE_{ST}) between S_1 and T_1 states is above 0.5 eV, organic compounds mostly exhibit fluorescence instead of phosphorescence. However, in the presence of heavy metal ions, the rate of intersystem crossing (ISC) can be enhanced due to spin–orbit coupling, which results in strong RTP with the process of $1 \rightarrow 2 \rightarrow 3 \rightarrow 6 \rightarrow 7$ as shown in Figure 1.8c. On the other hand, thermally TADF with the process of $1 \rightarrow 2 \rightarrow 3 \rightarrow 4 \rightarrow 5$ involves radiative transition of excitons from the S_1 state with a longer lifetime than the prompt fluorescence. TADF occurs through the reverse intersystem crossing (RISC) of the excitons from T_1 to S_1 states. In generally, the S_1 state is usually located above the T_1 state; hence, RISC process is an endothermic process which renders the TADF process to occur at high temperature.

Below we would discuss MPLMs by taking example of various pure organic materials and materials composed of molecular hybrids such as (i) inorganics/organics, (ii) organics/organics, and (iii) organics/polymer systems.

1.3.2.1 Organics PLMs

Pure OPLMs have the advantagesof wide variety, appreciable stability, high biocompatibility, and good processability. They have widespread applications in photobiology and optoelectronics, such as organic LEDs (OLEDs) and biological imaging. However, the inefficient spin–orbit coupling results in weak PersL in most of the cases. Researchers are therefore constantly giving efforts to enhance RTP and TADF using various approaches, such as rational design of molecular structures, careful crystallization, embedding into suitable matrixes, and so on. The first report on organic PersL based on TADF mechanism was reported from eosin in 1961, and its PersL was named as "E-type" delayed fluorescence (DF) (Figure 1.8) [94]. Later, Adachi et al. brought the concept of TADF for harvesting both singlet and triplet excitons in OLEDs by applying short electrical pulse excitation on a Sn(iv)–porphyrin complex [95]. They also demonstrated that a small ΔE_{ST} as required for efficient TADF can be achieved by a molecular structure design strategy to reduce the overlap of the molecule's highest occupied molecular orbital (HOMO) and lowest unoccupied molecular orbital (LUMO) in 2011 [96]. They achieved a ΔE_{ST} as small as 0.11 eV by constructing molecules with steric hindrance of bulky substituents as a twisted electron donor–acceptor (D–A) structure, for example, PIC-TRZ as shown in Figure 1.8b, to result in efficient TADF.

1.3.2.2 Organic–Inorganic Metal Halide Hybrid PLMs

Incorporation of heavy atoms intomolecular systems changes their photophysical and/or photochemical parameters due to the spin–orbit coupling of electronic states, which is known as the heavy atom effect [97]. In 1976, Winefordner et al.

demonstrated how external heavy atoms can help to achieved long-lived RTP in many compounds. For example, introduction of halogen atoms (such as I or Br) generally enhances the PersL of metal-free organic systems [14, 98]. Hybrid perovskites, which are formed by combining organic and inorganic semiconductors at the molecular scale, exhibit high luminescence efficiency and carrier mobility and are emerging for potential optoelectronics applications. Yang et al. demonstrated that doping of fluorophores into hybrid perovskites can inhibit the T–T annihilation process, and thereby act as a promising strategy for designing highly efficient MPLMs [99]. Ema et al. demonstrated that strong PersL can be achieved through energy transfer to the T state in organic–inorganic hybrid quantum-well structure consisting of perovskite-type lead bromide well layers and naphthalene-linked ammonium barrier layers. More specifically, an efficient energy transfer occurs from the inorganic cations in the perovskite to the T state of the organic naphthalene derivative cations [100].

1.3.2.3 Inorganic–Organic Molecular Hybrid PLMs

This class of MPLMs are based on metal–organic frameworks (MOFs), which consist of networks of metal clusters or metal ions connected by organic ligands. As luminescent MOFs containing noble-metal and rare-earth elements such as Au, Pt, Ru, Ir, Tb, and Eu typically exhibit phosphorescence with lifetimes starting from microseconds to milliseconds, rational design of novel MOFs to obtain long-lived PersL is a challenging task [14]. The RTP exhibited in MOFs can be tuned by using different stackings of organic ligands and alternation of metal ions. For example, the phosphorescence lifetimes of the two different two-dimensional (2D) layered Cd-based MOFs [14], which were synthesized through a hydrothermal process and stabilized by both interlayer π–π and C–H$\cdots$π interactions, can be enhanced up to seconds by changing the stacking modes of the organic ligands and organic–metal coordination environment. Recently, various rare earth ion-containing MOFs such as Eu-MOFs and Tb-MOFs with long red and green phosphorescence lifetimes have been developed [93]. Moreover, it has been observed that the Cd-doped Ln-MOF systems such as Cd–Tb-MOF and Cd–Eu-MOF have longer lifetimes than the Eu/Tb-based MOFs. This is due to the RTP energy transfer from T_1 to a higher level of Tb^{3+} and Eu^{3+} as shown in Figure 1.8d. Furthermore, by comparing the energy levels of the lowest singlet excited state S_1 and the lowest triplet excited state T_1 with the higher energy level of Tb^{3+} and Eu^{3+} ions, it can find why Tb^{3+} is better than Eu^{3+} in terms of sensitization with higher energy transfer efficiency and a longer lifetime [101].

1.4 Synthesis Methods for IPLMs

Except additional traps required for the presence of PersL phenomenon, IPLM matrices are the same as those non-IPLMs. Therefore, typically similar methods are used to prepare IPLMs with only slight change of synthesis conditions so that efficient traps are formed. Figure 1.9 gives a pictorial representation of various

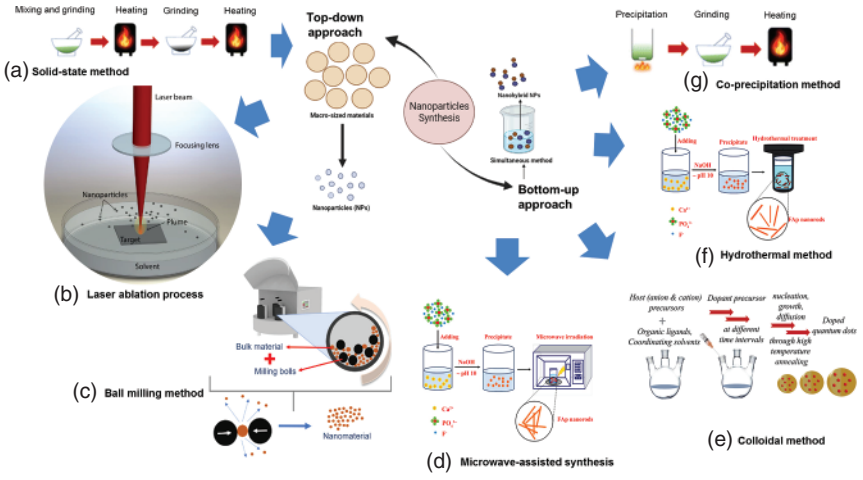

Figure 1.9 Pictorial representation of various top-down and bottom-up synthesis methods. Source: Adapted from Mujahid et al. [102] (a) solid-state method. Source: Adapted from Price et al. [103], (b) laser ablation process. Source: Adapted from Fernández-Arias et al. [104], (c) ball milling method. Source: Adapted from Barizão et al. [105], (d) microwave-assisted synthesis. Source: Adapted from Girija et al. [106], (e) colloidal method. Source: Adapted from Makkara and Viswanatha [107], (f) hydrothermal method. Source: Adapted from Duraisamy et al. [108], and (g) coprecipitation method. Source: Adapted from Price et al. [103].

synthesis methods for IPLMs, which are discussed elaborately below, while the synthesis of MPLMs will be discussed in Chapter 10.

1.4.1 Solid-State Method

The most widely usedmethod for synthesizing IPLMs is solid-state reactions at high temperatures owing to the advantage of simplicity and the ease of changing synthesis conditions. At first, solid precursors are mixed in required stoichiometric ratios and then intimately ground to maximize the contact between the precursors' particles. The mixed and ground precursors are then placed inside a tube or muffle furnace and heated up to a temperature that is sufficient to induce solid-state reactions but below the melting temperature of final IPLM compounds. Since heating close to or 200–300 °C below the melting temperature always leads to a dense, strongly agglomerated, and large grain size of final IPLM compounds, a postsynthesis grinding either manually or by using a ball mill is required for their practical applications as IPLMs. Choosing right temperatures for heating, which are sufficient for solid-state reactions and crystallization but do not lead to excessive sintering is therefore essential. Even if the final IPLM compounds become partly agglomerated, they can be separated using mild grinding. On the other hand, sintering might be advantageous as it may help get pore-free ceramics and thereby make IPLMs highly efficient because a large volume of scatter-free IPLM samples would be excited [109].

There are many examples where fluxes are also used in solid-state reactions of IPLMs, that is, inorganic salts such as chlorides and fluorides melt in between

precursor particles and facilitate their easier interdiffusion [110, 111]. Generally, the inorganic salts do not take part in the solid-state reactions of IPLMs; however, there are a few reported cases wherein fluxes get partly incorporated into the IPLM products and changed their PersL characteristics [112]. For example, when boric acid is used as the flux to prepare $SrAl_2O_4:Eu^{2+},Dy^{3+}$, boron creates mainly F-center related deeper traps and get stabilized by the incorporated B atom [113].

While heating time and temperature have a high impact on the performance of IPLMs, the heating atmosphere also can significantly influence their PersL properties. For example, if Eu^{2+} is the preferred valence state in a PLM, then it is essential to perform the thermal treatment in a reducing atmosphere. Otherwise, there is a high chance that Eu^{2+} can be oxidized to Eu^{3+} when heated in air, which leads to different PersL characteristics [114]. Similarly, for sulfides-based PLMs, synthesis in H_2S atmosphere is typically required. These atmospheric conditions can influence the trap density and characteristics, which are mostly related to various intrinsic defects such as oxygen or sulfur vacancies.

1.4.2 Ball Milling Method

Although solid-state reactions become the benchmark method for the synthesis of IPLMs with optimum performance, this method yields particles in the micrometer range in most cases. This limits the application of IPLM products in many areas, for instance, bio-imaging applications require the particle size of IPLMs in the nanometer range rather than the micrometer range. In such case, solid-state reaction method does not fulfill the requirement unless there is an effective way to decrease the particle size of IPLMs to the nanometer level. Ball milling is a top-down approach to reduce the particle size of IPLMs by mechanical impact and friction using planetary ball milling. Like manual grinding using a mortar and pestle, ball milling is also highly dependent on the size and hardness of starting IPLM materials. In many cases, a wide range of particle sizes of IPLM products are achieved. To get monodispersed particles, some kind of size selection is required. In the meantime, it has been observed that strong milling is detrimental to the PersL properties of IPLMs as it is difficult to avoid amorphization of their host matrices and oxidation of dopants due to surface exposure [115]. A postmilling thermal "healing" treatment at optimum temperatures that avoid particle growth and sintering can remove some of the side effects of ball milling.

1.4.3 Pulsed Laser Ablation Method

Pulsed laser ablation is another top-down method to reduce the size of bulk targets to nanoscale with the same chemical composition. In general, a pulse laser such as pulsed Nd:YAG laser of 1064 nm at 10 Hz can deliver a large amount of energy to the surface of targets like $SrAl_2O_4:Eu^{2+},Dy^{3+}$ pellet in acetone or ethanol. This creates a high impact pressure on the surface of $SrAl_2O_4:Eu^{2+},Dy^{3+}$ pellet to produce $SrAl_2O_4:Eu^{2+},Dy^{3+}$ NPs of ~7.5 nm with a narrow size distribution. This low-cost top-down method has already been used to produce IPLM nanoparticles (NPs) [116].

It is also possible to control the morphology of the IPLM NPs by properly adjusting pulse energy, laser wavelength, pulse frequency, and pulse width.

1.4.4 Solution-Based Methods

To overcome the limitation of solid-state reactions like difficult controlling particle size, morphology and dispersion of IPLMs, bottom-up synthesis can easily prepare PersL nanophosphors. Various solution-based methods including hydrothermal synthesis, sol-gel synthesis, colloidal synthesis, and coprecipitation always make nanosized particles with excellent morphology and size distribution. Unlike solid-state method wherein precursors need to react by solid diffusion, the solution-based methods involve intimate mixing of precursors on a molecular level. The particle size of the final IPLM products can be controlled by changing various synthetic conditions, such as pH, reaction temperature and time, precursor concentrations, and so on. Many IPLMs prepared by solution-based methods need postannealing treatment, which is often considered as a prerequisite to get sufficient PersL. On the other hand, annealing-free nanophosphors are flexible for surface functionalization when used for biological applications. Therefore, many new approaches to synthesize efficient PersL nanomaterials are emerging [117]. To get satisfactory PersL results, some specific methods have been developed for postannealing of preformed IPLM NPs while avoiding grain growth during thermal annealing. For example, by temporarily or permanently embedding IPLM NPs in a silica matrix as a template, the thermal annealing process can be performed [118]. Recently, we have developed a molten salt postannealing process to prepare monodispersed and bright PersL $ZnGa_2O_4:Cr^{3+}$ NPs with minimal agglomeration. It was demonstrated that mixing PersL NPs with molten salts can ensure good spatial isolation between adjacent nanomaterials during annealing, resulting in significantly enhanced luminescence with well-preserved morphology [119]. The solution-based synthesis methods are described below.

1.4.4.1 Hydrothermal Method

Among the solutions-based methods, hydrothermal method is one of the most widely used synthesis approach for preparing a variety of luminescence nanomaterials with controlled size and morphology. The luminescence nanomaterials can be prepared in a wide temperature range. This method possesses several advantages over the others, such as it can generate nanomaterials that are not stable at elevated temperature. Further, the morphology of the materials can be controlled by varying the synthesis parameters such as low-pressure or high-pressure conditions depending on the vapor pressure of the main composition in the reaction. In many cases of the synthesis of IPLMs, a post-heat treatment is necessary to generate PersL [120]. There are many reports that PersL can be improved by fine-tuning their nucleation kinetics and crystal size through controlled urea precipitation, and adjusting the Zn/Ga precursor ratio, and addition of ammonium nitrate, such as for hydrothermally synthesized ZnGa2O4:Cr^{3+} NPs [121].

1.4.4.2 Coprecipitation Method

Coprecipitation and thermal decomposition are common approaches for synthesizing metal oxide and fluoride NPs. For example, PersL nanophosphors of yttrium–aluminum–gallium garnet (YAGG) co-doped with Ce^{3+}, Cr^{3+}, and Pr^{3+} with various sizes were obtained by coprecipitation method followed by annealing at different temperature. It was observed that YAGG nanophosphor annealed at 1100 °C showing an acceptable degree of particle agglomeration and suitable for practical applications [122]. Likewise, $CaTiO_3:Pr^{3+}$ nanoparticles showing PersL characteristics with sizes ranging from 6 to 95 nm were prepared by a coprecipitation technique. Maximum phosphorescence occurred with increasing annealing temperature at 700 °C. The enhancement of PersL characteristics with increasing annealing temperature was due to a reduced surface-to-volume ratio, which decreased the surface defects acting as nonradiative recombination centers and increased the $^1D_2$–$^3H_4$ emission efficiency [123].

1.4.4.3 Colloidal Method

Among the bottom-up approaches, colloidal synthesis of PersL NPs was found to be more efficient in controlling the size, morphology, heterostructures, and optical properties of PersL NPs. For example, uniform X-ray-excitable PersL $Na(Gd,Lu)F_4:Ln^{3+}$ (Ln = Ce, Eu, Tb) NPs were first reported to be synthesized using this method by Cooper et al. in 2018 [39]. The method involves high-temperature coprecipitation of lanthanide fluoride using a noncoordinating solvent 1-octadecene (as the primary solvent) in combination with oleic acid (as a passivating ligand to prevent agglomeration) to direct nanoparticle growth. This method yields PersL NPs with very narrow size distributions and uniform morphology. The colloidal synthesis can also produce PersL heterostructured core-shell NPs. For example, CaF_2:Dy PersL NPs can be obtained through the colloidal synthesis method involving thermolysis of calcium trifluoroacetate in a fine-controllable manner. Furthermore, PersL heterostructured core–shell CaF_2:Dy@$NaYF_4$ NPs can be constructed in a controllable manner through this method due to excellent compatibility of CaF_2 crystal lattice with cubic phase $NaYF_4$ [21].

1.4.4.4 Template Method

Another accurate way to control the size and morphology of IPLM NPs is to use a template such as textured substrate or 3D porous structure to prepare them. For example, mesoporous silica nanospheres have been widely used to prepare various monodispersed IPLM NPs with well-preserved morphology such as SiO_2@$SrMgSi_2O_6:Eu^{2+},Dy^{3+}$ and SiO_2@$ZnGa_2O_4:Cr^{3+}$ [124, 125].

1.4.4.5 Other Methods

Apart from the synthesis methods described above, there are many other solution-based methods available for synthesizing IPLMs, wherein the high temperature required for solid-state reaction or precursor decomposition can be avoided if liquid precursors are used in a solvothermal or hydrothermal process, or in a microwave-assisted synthesis. Combustion synthesisis another method to

prepare IPLMs and their NPs, while the reactions may be very fast and sometimes hard-to-control. Despite many drawbacks, solid-state reactions are still the most widely employed method to prepare efficient IPLMs with desirable PersL performance. However, for bio-medical applications requiring monodispersed PLM NPs, bottom-up synthesis methods using liquid precursors are better suited. So far, the challenge to balance the small particle size and PersL intensity of IPLMs still remains a main issue.

1.4.5 PersL Glass, Glass Ceramics and Composites

Most of IPLMs prepared by the aforementioned methods are in powder form. However, for practical application such as in emergency signaling like the exit and fire extinguisher boards, they require additional processing to enable maneuvering and device project. One strategy is to employ functional composites by dispersing IPLMs powders homogeneously in polymer hosts like poly(methyl methacrylate) (PMMA). Although PMMA is able to keep a good percentual of its optical transparency, it undergoes several mechanical damages due to long exposure to UV light, which are difficult to restore with any treatment.

On the other hand, glasses such as phosphate and fluorophosphate glasses possess good resistance to high-energy radiation exposure and even though some defects are generated due to long exposure to high-energy radiation. Such defects can be easily healed after a thermal treatment. Moreover, phosphate glasses possess high chemical, thermal, and mechanical stability in addition to having extensive optical transmission in the wide UV to near-infrared spectrum region. Therefore phosphor-in-glass (PiG) composites make good alternatives to PMMA composites. The ILPMs can be embedded into glass hosts by their direct doping into them using melting-quenching technique, also known as "frozen sorbet method." For example, PersL $Sr_2MgSi_2O_7:Eu^{2+},Dy^{3+}$ (SMSO) polycrystalline material was embedded into the $80NaPO_3–20Ga_2O_3$ compositional glass system. Source: Adapted from Merízio et al. [126].

1.5 Measurements and Characteristics of PersL

The three major factors that regulate PersL output are the excitation, emission, and duration of PersL. While the PersL emission profile and decay profile can be measured using a convention emission spectroscopy after ceasing the excitation, the measurement of PersL excitation is a much more difficult process to detect and grasp. This is because of the fact that if someone measures PersL excitation spectrum in conventional excitation spectroscopy, then it is not certain whether the spectrum is originating due to excitation of PersL or only that of conventional luminescence. Furthermore, a strong PersL will make the conventional luminescence spectrum flattened down because of high background and low signal-to-noise ratio. Below we have discussed the measurement of the PersL excitation and emission for PLMs and their characteristics.

1.5.1 Excitation and Emission Characteristics

Many PLMs are often charged using UV or visible light with energies lower than the band gap energy of host matrices. However, when ionizing radiation such as X-rays is used, it is possible to fill different traps simultaneously unlike optical charging. This is attributed to the creation of an avalanche of delocalized electron–hole pairs by the high-energy X-rays. On the other hand, optical charging occurs through direct excitation of activators or through band-to-band excitation. Figure 1.10a shows the charging process followed by the decay profiles of $CaS:Eu^{2+},Dy^{3+}$ phosphor. The charging was carried out with 456 nm of excitation wavelength,

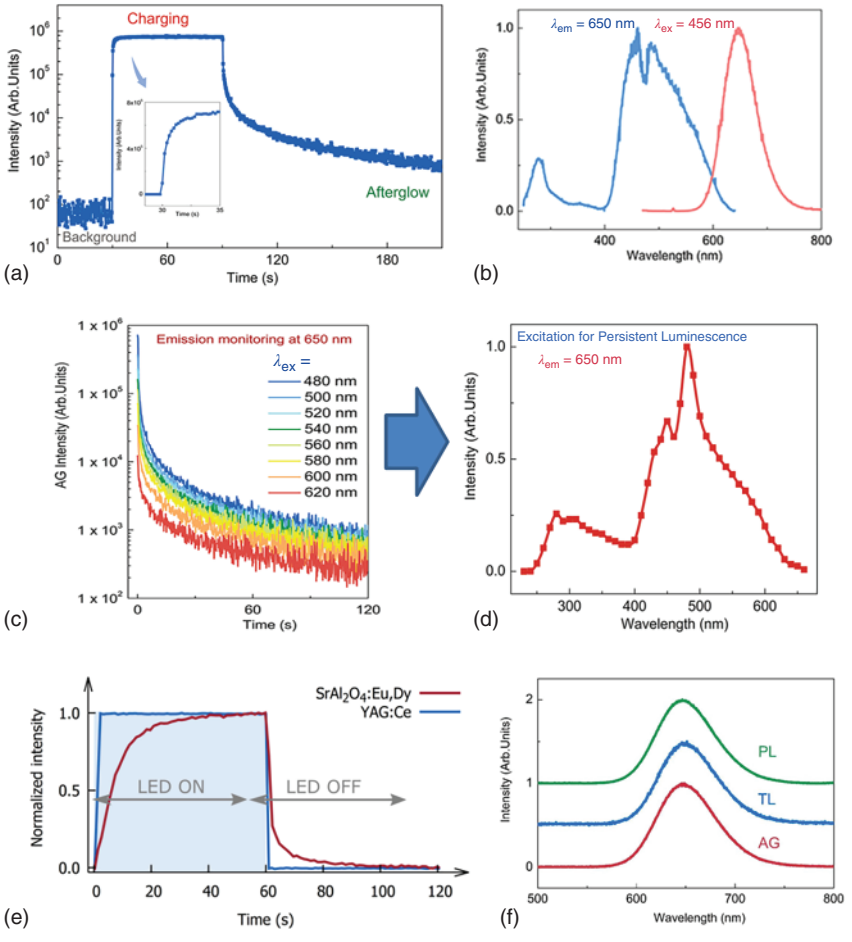

Figure 1.10 (a) Charging and afterglow decay profiles of $CaS:Eu^{2+},Dy^{3+}$ phosphor with 650 nm as the monitoring emission wavelength. Inset shows the starting points of the charging process. (b) PL excitation and emission spectra. (c) PersL decay profile at various excitation wavelengths of and the emission wavelength of 650 nm. (d) PersL excitation spectrum. Source: Adapted from Du and Poelman [127]. (e) Comparison of charging and decay profiles of a normal $Y_3Al_5O_{12}:Ce^{3+}$ phosphor and the benchmark PLM of $SrAl_2O_4$:Eu,Dy. Source: Adapted from Heggen et al. [128]. (f) Comparison of PersL (or afterglow, AG) and TL of $CaS:Eu^{2+},Dy^{3+}$. Source: Adapted from Du and Poelman [127].

whereas the light emission during charging and afterglow was monitored at 650 nm according to excitation and emission maxima of the photoluminescence (PL) given in Figure 1.10b. As shown in the inset of Figure 1.10a, the initial enhancement of light emission intensity originates due to combination of steady-state PL and afterglow emission of CaS:Eu^{2+},Dy^{3+}. During this time interval some of the excited electrons are getting stored in the traps while the others are coming back to the ground state of the activators and resulting PL. Due to continuous excitation process, when the rates of trapping and detrapping of the charge carriers are the same, a steady state with stable light output is achieved and resulting a flat line in charging spectra. When the excitation source is ceased, it will generate afterglow as shown in the decay profile. During this time, only the detrapping process occurs. However, the PL excitation maxima are not always the most efficient charging wavelength. One needs to measure the PersL excitation spectra for that. This can be done by measuring the decay profile at various wavelengths of excitation. For example, the decay profiles of CaS:Eu^{2+},Dy^{3+} can be monitored at 650 nm after one-minute excitation with monochromatic light starting from 230 to 660 nm with an interval of 10 nm. The PersL excitation spectrum can then be constructed by plotting the intensity at 650 nm as a function of the excitation wavelength. Figure 1.10c shows the PersL decay profiles at various excitation wavelengths, while Figure 1.10d shows the PersL excitation spectra at 650 nm wavelength of emission. The PersL excitation spectrum shows that the most efficient charging wavelength for this ILPM is ~480 nm.

Thus, PersL excitation spectra (or trap-filling spectra) generally provide the chargeable wavelength range of PLMs. One major difference between PL and PersL excitation processes of a PLM is that PL excitation spectra can be generated by using low energy light as excitation source (e.g. red light as excitation source for NIR PLMs), but in most cases, low energy light would not be able to charge the traps effectively for PersL, which rather requires higher energy photons. For example, although $LiGa_5O_8$:Cr^{3+} shows three different broad excitation bands in the UV, blue, and red regions for PL, only UV band can efficiently charge its traps and subsequently generate PersL [129]. Figure 1.10e shows the comparison of charging and decay profiles of a normal $Y_3Al_5O_{12}$:Ce^{3+} phosphor and the benchmark PLM of $SrAl_2O_4$:Eu,Dy. As discussed earlier, the light output in the case of PLMs, PersL intensity increases to the maximum only after a sufficiently long illumination time, a dynamic equilibrium of trap filling by the illumination and emptying traps by the room temperature thermal energy, or by optically stimulated luminescence using the same source. Since there are no tarps in the normal phosphors, their light output reaches the maximum immediately once the charging process is initiated. On the other hand, since the normal phosphor does not show any PersL and having a very fast decay, its light output intensity immediately comes down to zero as the excitation source is turned off. In contrast, a PLM keeps on emitting light after ceasing the excitation source. Figure 1.10f showed the comparison of emission spectra generated due to PL, PersL (or afterglow) and TL of CaS:Eu^{2+},Dy^{3+}. It was observed that the PersL and TL spectra are very similar to the steady-state PL. This suggests that all emissions originate from the same activator, that is, Eu^{2+} ions.

1.5.2 Trap Properties

1.5.2.1 Trap Depth and Optimum Temperature for Potential Applications

It is now well understood that the deeper the trap depth and the higher the energy barrier, the more heat is required to release the charge carriers from the traps of PLMs. The shallow traps, which are very close to CB or VB, are emptied very fast at room temperature. In contrast, deep traps are rarely emptied at room temperature and show PersL only at elevated temperatures. Therefore, temperature-dependent PersL of PLMs is largely determined by the trap depth profile of existing traps and their possible distribution in the host matrices. Trap depth is generally determined by TL experiment which is based on the emission read-out of a preirradiated IPLM sample caused by the constant heating wherein the thermal energy liberates the excited charge carriers from the traps. As shown in Figure 1.11a, TL glow curves can be obtained by plotting TL emission intensity (I) versus heating temperature (T). The various peaks in the glow curves reveal the existence of various traps at their corresponding thermal energy or trap depths (shallow or deep), which are responsible for PersL. Therefore, trap depths can be evaluated via the initial rise analysis of glow curves. As shown in Figure 1.11a, the deep traps are appeared at higher temperature in the TL glow curve, which is due to their higher tarp depth. In other words, higher thermal energy is required to release the charge carriers from deep traps.

The temperature dependent PersL characteristic of a PLM determines its application eligibility in various environmental conditions. This has led to the concept of the optimum working temperature, $T_{optimum}$ at which the maximum PersL output of a PLM is achieved within a reasonable time frame [130]. It has been observed that most commercial ILPMs have $T_{optimum}$ at around room temperature, which ensures a large number of room-temperature applications like emergency lighting, decoration, safety signage, and night-vision surveillance. The $T_{optimum}$ can be determined by the difference between two TL read-out events (TL_1–TL_2), with and without fading, as a function of ambient temperature. For example, Figure 1.11b,c represents the TL glow curves of IPLM of CaS:Eu^{2+},Dy^{3+} without fading and with 30 minutes of fading between irradiation and heating stage. While the PersL decay profiles at various temperature in Figure 1.11d show optimum performance around −20 °C, the $T_{optimum}$ is also found to be at a low temperature range, around −20 °C as shown in Figure 1.11e. This suggests that this PLM is more suited for low-temperature operation. Therefore, researchers need to focus on the trap depth engineered of PLMs carefully before designing them for particular applications at a certain temperature range.

1.5.2.2 Controlling Trap Filling and Releasing Kinetics by Temperature and Pump Power

Both trap filling and releasing processes by charge carriers co-exist in PLMs during the charging process. Owing to their low thermal barrier, shallow traps are much more easily depopulated than deep traps. Thus, the occupancy of traps can be varied by performing charging process at different temperatures. For example, at a low temperature which is above the thermal barrier, both shallow and deep

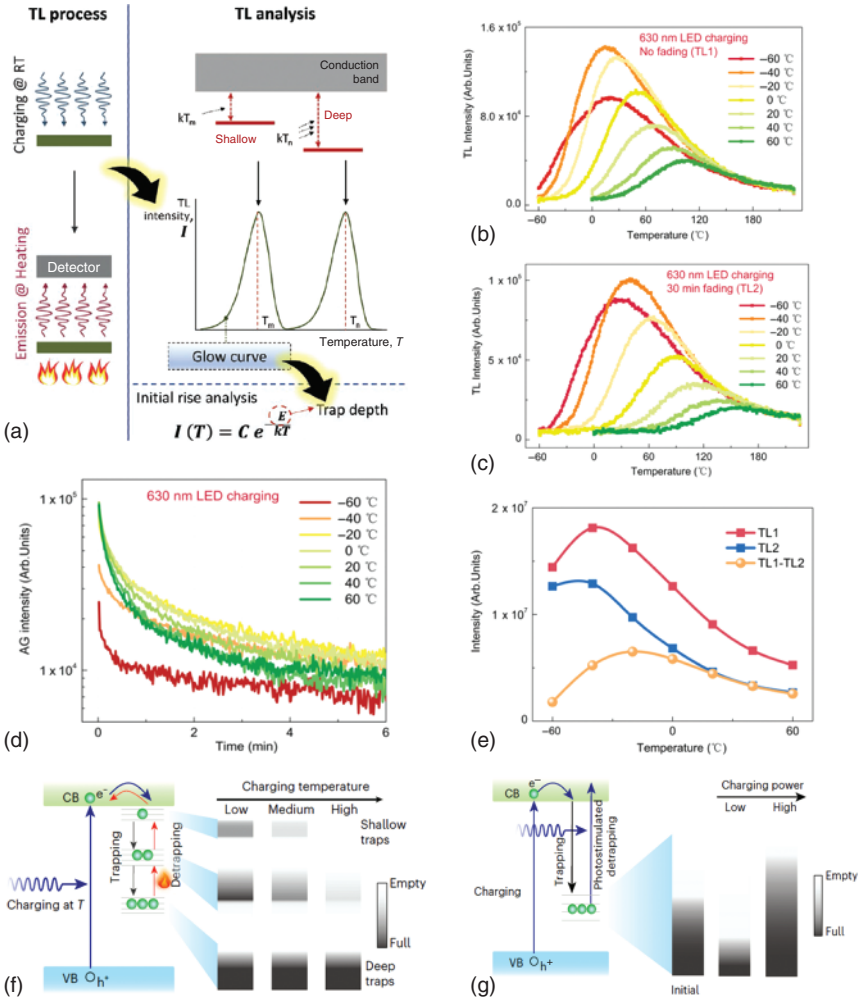

Figure 1.11 (a) Pictorial representation of trap depth's analysis through TL measurement and TL study. TL measurement can be carried out after charging IPLMs at room temperature followed by monitoring the emission upon continuous heating. Source: Adapted from Wang and Mao [46]. TL glow curves of PersL CaS:Eu^{2+},Dy^{3+} phosphor: (b) without fading and (c) with 30 minutes fading between irradiation and heating stage. (d) PersL decay profiles at various temperatures. (e) Measurement of $T_{optimum}$. Source: Adapted from Du and Poelman [127]. Control of trap filling by manipulation of (f) charge temperature T and (g) power density, respectively. Source: Adapted from Liang et al. [29]/Springer Nature.

traps can be filled. However, as the temperature is increased, the charge carriers in shallow traps become unstable against strong thermal stimulation. In contrast, the charge carriers in deep traps are stable. They become unstable only at very high temperature, that is, until the thermal stimulation matches their thermal barrier (Figure 1.11f). Therefore, due to the well-preserved characteristics of shallow traps at low temperature, slightly higher PersL can be achieved when PLMs are charged

at low temperature instead of high temperature, which results in depletion of both shallow and intermediate traps.

At a particular excitation wavelength, TL spectra of PLMs do not vary appreciably by changing the excitation's power, suggesting a constant occupation of different traps for particular excitation energy. However, if different excitation sources are used, then different occupancy of traps is observed for a particular PLM due to their different trap filling and de-trapping capabilities. For instance, when $LaMgGa_{11}O_{19}:Cr^{3+}$ is charged using a 450 nm blue LED, its trapped charge carriers can partially escape from the traps by absorbing the same 450 nm excitation photons, which results in photo-induced trap depletion [131]. Since the de-trapping process outperforms the trapping process at low-power pumping, pumping at high power is required so that trapping rate can exceed the release rate and a saturation of charge carriers is achieved in order to generate intense and long-lasting PersL (Figure 1.11g).

1.5.2.3 PersL Lifetime and Storage Capacity

Usually, the performance of a PLM is evaluated by measuring the time dependency of PersL intensity following the irradiation of the PLM using a standard light source for a certain time. Since visible and NIR lights have different eye sensitivity, the units used to report these PersL curves are different. The PersL curves of visible PLMs are usually expressed in photometric units. However, since the emission spectra of NIR PLMs fall outside the spectral range of the eye sensitivity, the units are expressed in radiometric units. The surface luminance for visible PLMs is specified in the photometric luminance as cd/m^2, while the radiometric equivalent of the photometric luminance is used for UV and NIR PLMs as $mW/m^2/sr$. The "PersL lifetime" is the time when a benchmark luminance of $0.32\,mcd/m^2$ is reached since the ceasing of the excitation source. In the PersL field, another benchmark luminance value of $0.30\,mcd/m^2$ is also often used. The storage capacity of a PLM is expressed as the number of photons emitted by one gram of phosphor during the phosphor's afterglow. This metric allows comparing storage capacity of PLMs independent of their spectral characteristics and morphology. For example, the storage capacity of the benchmark $SrAl_2O_4$:Eu,Dy PLM has been determined to $(1.57 \pm 0.03) \times 10^{17}$ photons/gram which is equal to ~1.6% of the Eu activators being ionized. This indicates that there is still needed improvement for this benchmark PLM [132]. The storage capacity can be measured in a fairly straightforward way. At first, PLMs are incorporated into a transparent polymer in order to excite all the PLM particles uniformly. Next, the PLMs are excited until saturation, or dynamic equilibrium is reached. Once the charging process is completed and the excitation source is turned off, the PersL curve of the PLM-containing polymer layer is started recording using a calibrated radiometric or photometric detector. As discussed earlier, PersL performance depends on the type of excitation sources being used and UV sources are more effective to fill all traps than visible and NIR sources. Therefore, it is necessary to mention the excitation source, its intensity, and the

spectral output, or more specifically, the parameters that are chosen to mimic the intended application for certain types of PLMs.

1.5.3 Trap Manipulation

As discussed earlier, trap manipulation holds the key for successful development of efficient PLMs and traps are created by various intrinsic lattice point defects, including vacancy and antisite defects, or impurity defects. In many cases, multiple-point defects can co-exist in matrices and create various types of traps with different trap depth profiles. Depending on trap depth or thermal barrier, some traps are involved in the trapping process of charge carriers while others are not. Vacancies such as cation and anion vacancies are created due to charge imbalance in matrices. These vacancies are often created simultaneously during the material synthesis of PLMs in equal numbers to maintain charge neutrality and are known as Schottky defects. Aliovalent substitution, that is, substituting lattice ions with ions of different valence, may create both positively and negatively charged defects. For example, doping Ge^{4+} and Mn^{4+} at Al^{3+} site in $LaAlO_3$ creates NIR PersL lasting for more than 20 hours due to the creation of both positively and negatively charged vacancies along with interstitial defects [133]. Similarly, nonstoichiometric synthesis of PLMs wherein the ionic stoichiometry of precursors is slightly changed before the synthesis generated Zn vacancies in $Zn_{2.94}Ga_{1.96}Ge_2O_{10}:Cr^{3+},Pr^{3+}$ [134]. The negatively charged Zn vacancies acted as hole traps and significantly increased the intensity and duration of NIR PersL.

Co-doping lanthanides is the most widely used strategy to generate electron and hole traps. As discussed in the band-engineering model (Figure 1.5c), where divalent lanthanides like Pr^{2+}, Nd^{2+}, Dy^{2+}, and Tm^{2+} with their ground states positioned just below the CB within the host band gap, their trivalent lanthanides, that is, Pr^{3+}, Nd^{3+}, Dy^{3+}, and Tm^{3+}, can serve as electron acceptors. In contrast, since the energy gap between the CB and ground state of Sm^{2+} and Yb^{2+} is high, Sm^{3+} and Yb^{3+} generate deep traps.

Other successful strategies include changing the sintering atmosphere or irradiating PLMs with high-energy rays, which are successful in generating desired traps. For example, when $Ca_2SnO_4:Gd^{3+},Eu^{3+}$ is sintered in a nonoxidizing atmosphere, oxygen vacancies are generated to act as efficient electron traps and yield much longer PersL than that sintered in air. Similarly, NIR PersL from $CaTiO_3:Cr^{3+}$ can only be generated when it is prepared in a reducing atmosphere to create oxygen vacancies [135]. In many cases, when PLMs are irradiated with high-energy photons, small anions can get displaced into interstitial sites, which create Frenkel defects acting as traps. For example, X-rays irradiation of lanthanide-doped fluorides can trigger hour-long PersL, which is attributed to the formation of fluoride vacancies acting as electron traps. High-momentum X-ray photons displace fluoride anions into interstitial sites during the elastic collisions [136]. Interestingly, when these X-ray irradiated PLMs are further heated

or irradiated with light, the displaced fluoride ions can diffuse back to their original sites and result in diminished PersL.

1.6 Summary and Challenges

In this introductory chapter of PersL, we have summarized the brief history of PLMs and their already established and possible future applications, various PersL mechanisms, fundamental understanding of various electron and hole traps, various types of PLMs and their synthesis procedures, and finally, some effective approaches to control traps to enhance the performance of PLMs. However, despite many substantial and rapid progresses in this class of emerging compounds, many challenges remain to be addressed for a clearer understanding before designing future PLMs. For example, defect centers within PLMs have both positive and negative impacts on their optical properties. In many cases, defect centers provide some nonradiative pathways to radiative centers, which thereby decrease the light yield of PLMs. Specifically, when the trap depth of defect-related traps is high, it will result in nonradiative transition to the VB instead of releasing the charge carrier to the CB (Figure 1.4c). Therefore, we must carefully avoid defects that provide nonradiative pathways. A thorough understanding of these defects or impurity-created energy levels inside the band gap of PLM host matrices is required before designing efficient PLMs. Furthermore, defects related traps should reproduce the PersL properties and should not disappear by changing atmospheric conditions.

Another major challenge of trap-controlled PLMs is the requirement of thorough characterization of these traps using multiple techniques. Multiple defects can exist in matrices and each of them can create separate traps. Therefore, the band-engineering model becomes more complex to understand. Since the energy position of point defects within the band gap of host matrices varies from one matrix to other, the trap depth of these defects also varies. Therefore, a similar defect, such as oxygen vacancy in oxide-based PLMs, may act as a shallow trap in one matrix but as a deep trap in another matrix due to the change of the band gap. Hence, it is difficult to construct a common band engineering model like that with the divalent and trivalent lanthanides. It is also essential to understand how the defects evolved in various matrices and the rate of capturing or releasing charge carriers from these trap states. A close collaboration between experimental and theoretical groups is required to understand the dynamic relationship between crystal structure, local electronic states, trap levels, and PersL properties.

References

1 Harvey, E.N. (1957). *A History of Luminescence from the Earliest Times Until 1900*. Philadelphia, PA: American Philosophical Society.
2 Yen, W.M. and Weber, M.J. (2004). *Inorganic Phosphors: Compositions, Preparation and Optical Properties*. Boca Raton, FL: CRC Press.
3 Yen, W.M., Shionoya, S., and Yamamoto, H. (2007). *Phosphor Handbook*, 2e. Boca Raton, FL: CRC Press.

4 Xu, J. and Tanabe, S. (2019). Persistent luminescence instead of phosphorescence: history, mechanism, and perspective. *J. Lumin.* 205: 581–620.

5 Yuan, L., Jin, Y., Su, Y. et al. (2020). Optically stimulated luminescence phosphors: principles, applications, and prospects. *Laser Photonics Rev.* 14 (12): 2000123.

6 Lastusaari, M., Laamanen, T., Malkamäki, M. et al. (2012). The bologna stone: history's first persistent luminescent material. *Eur. J. Mineral.* 24: 885.

7 Hoogenstraaten, W. and Klasens, H.A. (1953). Some properties of zinc sulfide activated with copper and cobalt. *J. Electrochem. Soc.* 100: 366.

8 Smet, P.F., Moreels, I., Hens, Z., and Poelman, D. (2010). Luminescence in sulfides: a rich history and a bright future. *Materials* 3: 2834.

9 Murayama, Y. (2006). *History of Persistent Phosphors in Japan*. Night-Vision Industry Association of Japan.

10 Matsuzawa, T., Aoki, Y., Takeuchi, N., and Murayama, Y. (1996). A new long phosphorescent phosphor with high brightness, $SrAl_2O_4$:Eu^{2+},Dy^{3+}. *J. Electrochem. Soc.* 143: 2670.

11 Smet, P.F., Botterman, J., Van Den Eeckhout, K. et al. (2014). Persistent luminescence in nitride and oxynitride phosphors: a review. *Opt. Mater.* 36: 1913.

12 Rojas-Hernandez, R.E., Rubio-Marcos, F., Rodriguez, M.Á., and Fernandez, J.F. (2018). Long lasting phosphors: $SrAl_2O_4$:Eu,Dy as the most studied material. *Renew. Sust. Energ. Rev.* 81: 2759.

13 Liu, Y., Li, C., Ren, Z. et al. (2018). All-organic thermally activated delayed fluorescence materials for organic light-emitting diodes. *Nat. Rev. Mater.* 3: 18020–18024.

14 Gao, R., Kodaimati, M.S., and Yan, D. (2021). Recent advances in persistent luminescence based on molecular hybrid materials. *Chem. Soc. Rev.* 50: 5564–5589.

15 Yang, Z., Mao, Z., Xie, Z. et al. (2017). Recent advances in organic thermally activated delayed fluorescence materials. *Chem. Soc. Rev.* 46: 915–1016.

16 Nemoto & Co., Ltd. (n.d.). Phosphorescent pigment. https://www.nemoto.co.jp/en/luminouspigment/ (accessed 27 November 2024).

17 Poelman, D., Van der Heggen, D., Du, J. et al. (2020). Persistent phosphors for the future: fit for the right application. *J. Appl. Phys.* 128: 240903.

18 Li, Y., Gecevicius, M., and Qiu, J. (2016). Long persistent phosphors—from fundamentals to applications. *Chem. Soc. Rev.* 45: 2090–2136.

19 Feng, A. and Smet, P.F. (2018). A review of mechanoluminescence in inorganic solids: compounds, mechanisms, models and applications. *Materials* 11 (4): 484.

20 Petit, R.R., Michels, S.E., Feng, A., and Smet, P.F. (2019). Adding memory to pressure-sensitive phosphors. *Light Sci. Appl.* 8 (1): 124.

21 Kersemans, M., Smet, P.F., Lammens, N. et al. (2015). Fast reconstruction of a bounded ultrasonic beam using acoustically induced piezo-luminescence. *Appl. Phys. Lett.* 107: 234102.

22 Pei, P., Chen, Y., Sun, C. et al. (2021). X-ray-activated persistent luminescence nanomaterials for NIR-II imaging. *Nat. Nanotechnol.* 16: 1011–1018.

23 Liang, L., Chen, N., Jia, Y. et al. (2019). Recent progress in engineering near-infrared persistent luminescence nanoprobes for time-resolved biosensing/bioimaging. *Nano Res.* 12 (6): 1279–1292.

24 Wu, S., Pan, Z., Chen, R., and Liu, X. (2017). *Long Afterglow Phosphorescent Materials*. Cham: Springer.

25 Xiong, P. and Peng, M. (2019). Recent advances in ultraviolet persistent phosphors. *Opt. Mater.: X* 2: 100022.

26 Zhou, Z., Li, Y., and Peng, M. (2020). Near-infrared persistent phosphors: Synthesis, design, and applications. *Chem. Eng. J.* 399: 125688.

27 Qiu, J., Li, Y., and Jia, Y. (2021). *Persistent Phosphors: From Fundamentals to Applications*. Woodhead Publishing.

28 Jin, H., Debroye, E., Keshavarz, M. et al. (2020). It's a trap! On the nature of localised states and charge trapping in lead halide perovskites. *Mater. Horiz.* 7: 397.

29 Liang, L., Chen, J., Shao, K. et al. (2023). Controlling persistent luminescence in nanocrystalline phosphors. *Nat. Mater.* 22: 289–304.

30 Dorenbos, P. (2005). Mechanism of persistent luminescence in Eu^{2+} and Dy^{3+} codoped aluminate and silicate compounds. *J. Electrochem. Soc.* 152: H107.

31 Ueda, J., Dorenbos, P., Bos, A.J.J. et al. (2015). Control of electron transfer between Ce^{3+} and Cr^{3+} in the $Y_3Al_{5-x}Ga_xO_{12}$ host via conduction band engineering. *J. Mater. Chem. C* 3: 5642.

32 Lyu, T. and Dorenbos, P. (2018). Charge carrier trapping processes in lanthanide doped $LaPO_4$, $GdPO_4$, YPO_4, and $LuPO_4$. *J. Mater. Chem. C* 6: 369.

33 Luo, H., Bos, A.J.J., and Dorenbos, P. (2016). Controlled electron–hole trapping and detrapping process in $GdAlO_3$ by valence band engineering. *J. Phys. Chem. C* 120: 5916.

34 Yamamoto, H. and Matsuzawa, T. (1997). Mechanism of long phosphorescence of $SrAl_2O_4$:Eu^{2+},Dy^{3+} and $CaAl_2O_4$:Eu^{2+},Nd^{3+}. *J. Lumin.* 72–74: 287–289.

35 Tanabe, S. and Hanada, T. (1996). Appearance of light-storage rare earth aluminate phosphors and their optical properties. *New Ceram.* 9: 27.

36 Takasaki, H., Tanabe, S., and Hanada, T. (1996). Long-lasting afterglow characteristics of Eu,Dy codoped SrO-Al_2O_3 phosphor. *J. Ceram. Soc. Jpn.* 104: 322.

37 Korthout, K., Van den Eeckhout, K., Botterman, J. et al. (2011). Luminescence and x-ray absorption measurements of persistent $SrAl_2O_4$:Eu,Dy powders: evidence for valence state changes. *Phys. Rev. B* 84: 085140.

38 Holsa, J., Aitasalo, T., Jungner, H. et al. (2004). Role of defect states in persistent luminescence materials. *J. Alloys Compd.* 374: 56–59.

39 Wang, L., Wang, C., Chen, Y. et al. (2022). Red-emitting $SrGa_2O_4$:Cu^{2+} phosphor with super-long persistent luminescence. *Chem. Mater.* 34: 10068–10076.

40 Zhuang, Y., Katayama, Y., Ueda, J., and Tanabe, S. (2014). A brief review on red to near-infrared persistent luminescence in transition-metal-activated phosphors. *Opt. Mater.* 36: 1907.

41 Katayama, Y., Kobayashi, H., and Tanabe, S. (2015). Deep-red persistent luminescence in Cr^{3+} doped $LaAlO_3$ perovskite phosphor for in vivo imaging. *Appl. Phys. Express* 8: 012102.

42 Liu, F., Yan, W., Chuang, Y.J. et al. (2013). Photostimulated near-infrared persistent luminescence as a new optical read-out from Cr^{3+}-doped $LiGa_5O_8$. *Sci. Rep.* 3: 1554.

43 Yang, T., Jiang, H., Hai, O. et al. (2021). Effect of oxygen vacancies on the persistent luminescence of $Y_3Al_2Ga_3O_{12}:Ce^{3+},Yb^{3+}$ phosphors. *Inorg. Chem.* 60 (23): 17797–17809.

44 Pan, Z., Lu, Y.Y., and Liu, F. (2012). Sunlight-activated long-persistent luminescence in the near-infrared from Cr^{3+}-doped zinc gallogermanates. *Nat. Mater.* 11: 58–63.

45 Clabau, F., Rocquefelte, X., Jobic, S. et al. (2005). Mechanism of phosphorescence appropriate for the long-lasting phosphors Eu^{2+}-doped $SrAl_2O_4$ with codopants Dy^{3+} and B^{3+}. *Chem. Mater.* 17: 3904–3912.

46 Wang, X. and Mao, Y. (2022). Emerging ultraviolet persistent luminescent materials. *Adv. Opt. Mater.* 10: 2201466.

47 Kang, F., Sun, G., Boutinaud, P. et al. (2021). Recent advances and prospects of persistent luminescent materials as inner secondary self-luminous light source for photocatalytic applications. *Chem. Eng. J.* 403: 126099.

48 Wang, X., Chen, Y., Liu, F. et al. (2020). Solar-blind ultraviolet-C persistent luminescence phosphors. *Nat. Commun.* 11: 2040.

49 Liu, Q., Feng, Z.Y., Li, H. et al. (2021). Non-rare-earth UVC persistent phosphors enabled by bismuth doping. *Adv. Opt. Mater.* 9: 2002065.

50 Wang, X., Chen, Y., Kner, P.A., and Pan, Z. (2021). Gd^{3+}-activated narrowband ultraviolet-B persistent luminescence through persistent energy transfer. *Dalton Trans.* 50: 3499.

51 Jin, Y.H., Hu, Y.H., Duan, H. et al. (2014). The long persistent luminescence properties of phosphors: Li_2ZnGeO_4 and $Li_2ZnGeO_4:Mn^{2+}$. *RSC Adv.* 4: 11360–11366.

52 Kitagawa, Y., Ueda, J., and Tanabe, S. (2022). Blue persistent phosphor of $YSiO_2N:Ce^{3+}$ developed by codoping Sm^{3+} or Tm^{3+} ions and thermoluminescence analysis of their trap distributions. *Phys. Status Solidi A* 219: 2100670.

53 Mei, Y., Xu, H., Zhang, J. et al. (2015). Design and spectral control of a novel ultraviolet emitting long lasting phosphor for assisting TiO_2 photocatalysis: $Zn_2SiO_4:Ga^{3+},Bi^{3+}$. *J. Alloys Compd.* 622: 908–912.

54 Wang, X. and Mao, Y. (2022). Recent advances in Pr^{3+}-activated persistent phosphors. *J. Mater. Chem. C* 10 (10): 3626–3646.

55 Yang, Y.M., Li, Z.Y., Zhang, J.Y. et al. (2018). X-ray-activated long persistent phosphors featuring strong UVC afterglow emissions. *Light Sci. Appl.* 7: 88.

56 Raeiszadeh, M. and Adeli, B. (2020). A critical review on ultraviolet disinfection systems against COVID-19 outbreak: applicability, validation, and safety considerations. *ACS Photonics* 7 (11): 2941–2951.

57 Yan, S., Liang, Y., Liu, J. et al. (2021). Development of ultraviolet-B long-lived persistent phosphors in Pr^{3+}-doped garnets. *J. Mater. Chem. C* 9: 14730.

58 Wang, X. and Mao, Y. (2021). Achieving ultraviolet C and ultraviolet B dual-band persistent luminescence by manipulating the garnet structure. *Adv. Opt. Mater.* 10 (5): 2102157.

59 Zhou, Z., Xiong, P., Liu, H., and Peng, M. (2020). Ultraviolet-A persistent luminescence of a Bi^{3+}-activated $LiScGeO_4$ material. *Inorg. Chem.* 59: 12920.

60 Sun, H., Gao, Q., Wang, A. et al. (2020). Ultraviolet-B persistent luminescence and thermoluminescence of bismuth ion doped garnet phosphors. *Opt. Mater. Express* 10: 1296.

61 Gutiérrez-Martín, F., Fernández-Martinez, F., Díaz, P. et al. (2010). Persistent UV phosphors for application in photo catalysis. *J. Alloys Compd.* 501: 193–197.

62 Sharma, S.K., Bettinelli, M., Carrasco, I. et al. (2019). Dynamics of charges in superlong blacklight-emitting CaB_2O_4:Ce^{3+} persistent phosphor. *J. Phys. Chem. C* 123: 14639.

63 Sonekar, R., Omanwar, S., Moharil, S. et al. (2009). Luminescence in $LaBaB_9O_{16}$ prepared by combustion synthesis. *J. Lumin.* 129: 624.

64 Yan, J., Ning, L., X., Huang, Y. C. et al. (2014). Luminescence and electronic properties of $Ba_2MgSi_2O_7$:Eu^{2+}: a combined experimental and hybrid density functional theory study. *J. Mater. Chem. C* 2: 8328–8332.

65 He, H., Fu, R.L., Song, X.F. et al. (2010). Observation of fluorescence and phosphorescence in $Ca_2MgSi_2O_7$:Eu^{2+},Dy^{3+} phosphors. *J. Electrochem. Soc.* 157: J69–J73.

66 Van den Eeckhout, K., Poelman, D., and Smet, P.F. (2013). Persistent luminescence in non-Eu^{2+}-doped compounds: a review. *Materials* 6: 2789–2818.

67 Takahashi, Y., Ando, M., Ihara, R., and Fujiwara, T. (2011). Green-emissive Mn-activated nanocrystallized glass with willemite-type Zn_2GeO_4. *Opt. Mater. Express* 1: 372–378.

68 Yu, Y., Wang, J., Wang, J. et al. (2017). Structural characterization and optical properties of longlasting $CaAl_2O_4$:Eu^{2+},Nd^{3+} phosphors synthesized by microwave-assisted chemical co-precipitation. *J. Rare Earths* 35: 652–657.

69 Chang, C.K. and Mao, D.L. (2004). Long lasting phosphorescence of $Sr_4Al_{14}O_{25}$:Eu^{2+},Dy^{3+} thin films by magnetron sputtering. *Thin Solid Films* 460: 48–52.

70 Zheng, M., Chen, X., Lei, B. et al. (2013). Synthesis and luminescence properties of flower-like $Sr_2MgSi_2O_7$:Eu^{2+},Dy^{3+} phosphor via hydrothermal-homogeneous coprecipitation route. *ECS Solid State Lett.* 2: R19–R22.

71 Lastusaari, M., Bos, A.J.J., Dorenbos, P. et al. (2015). Wavelength-sensitive energy storage in $Sr_3MgSi_2O_8$:Eu^{2+},Dy^{3+}. *J. Therm. Anal. Calorim.* 121: 29–35.

72 Yamaga, M., Ohsumi, Y., Nakayama, T., and Han, T.P.J. (2012). Persistent phosphorescence in Ce-doped Lu_2SiO_5. *Opt. Mater. Express* 2: 413–419.

73 Wang, X., Jia, J.D.D., and Yen, W.M. (2003). Mn^{2+} activated green, yellow, and red long persistent phosphors. *J. Lumin.* 102: 34–37.

74 Dai, W.B. (2014). Investigation of the luminescent properties of Ce^{3+} doped and Ce^{3+}/Mn^{2+} co-doped $CaAl_2Si_2O_8$ phosphors. *RSC Adv.* 4: 11206–11215.

75 Pang, R., Jia, Y., Zhao, L. et al. (2014). Tunable long lasting phosphorescence due to the selective energy transfer from defects to luminescent centres via tunnelling in Mn^{2+} and Tm^{3+} co-doped zinc pyrophosphate. *Dalton Trans.* 43: 9661–9668.

76 Zeng, W., Wang, Y.H., Han, S.C. et al. (2013). Design, synthesis and characterization of a novel yellow long-persistent phosphor: $Ca_2BO_3Cl:Eu^{2+},Dy^{3+}$. *J. Mater. Chem. C* 1: 3004–3011.

77 Xu, J., Ueda, J., Zhuang, Y.X. et al. (2015). $Y_3Al_{5-x}Ga_xO_{12}:Cr^{3+}$: a novel red persistent phosphor with high brightness. *Appl. Phys. Express* 8: 042602.

78 Che, G.B., Li, X.Y., Liu, C.B. et al. (2008). Long-lasting phosphorescence properties of Mn^{2+}-doped $Cd_2Ge_7O_{16}$ orange light-emitting phosphor. *Phys. Status Solidi A* 205: 194–198.

79 Wang, F., Yang, B., Liu, D.C. et al. (2014). Influence of vacuum upon preparation and luminescence of Si^{4+} and Ti^{4+} co-doped Gd_2O_2S:Eu phosphor. *Spectrochim. Acta Part A* 126: 46–52.

80 Hang, T., Liu, Q., Mao, D.L., and Chang, C.K. (2008). Long lasting behavior of $Gd_2O_2S:Eu^{3+}$ phosphor synthesized by hydrothermal routine. *Mater. Chem. Phys.* 107: 142–147.

81 Li, Y.J., Wang, M.W., Zhang, L.D. et al. (2013). Soft chemical synthesis and luminescence properties of red long-lasting phosphors $Y_2O_2S:Sm^{3+}$. *Int. J. Miner. Metall. Mater.* 20: 972–977.

82 Cui, C.E., Jiang, G.W., Huang, P. et al. (2014). Synthesis and characterization of $Y_2O_2S:Eu^{3+},Mg^{2+},Ti^{4+}$ nanotubes via hydrothermal method. *J. Lumin.* 145: 665–668.

83 Jin, Y.H., Hu, Y.H., Chen, L. et al. (2013). Luminescence properties of dual-emission (UV/visible) long afterglow phosphor $SrZrO_3:Pr^{3+}$. *J. Am. Ceram. Soc.* 96: 3821–3827.

84 Noto, L.L., Pitale, S.S., Gusowki, M.A. et al. (2013). Afterglow enhancement with In^{3+} co-doping in $CaTiO_3:Pr^{3+}$ red phosphor. *Powder Technol.* 237: 141–146.

85 Boutinaud, P., Sarakha, L., and Mahiou, R. (2009). $NaNbO_3:Pr^{3+}$: a new red phosphor showing persistent luminescence. *J. Phys.:Condens. Matter* 21: 025901.

86 Liu, Z.R. and Zhong, R.X. (2013). Green and red long lasting phosphorescence (LLP) in γ-$Zn_3(PO_4)_2:Mn^{2+}/Ga^{3+}$. *J. Alloys Compd.* 556: 6–11.

87 Lei, B.F., Man, S.Q., Du, Y.L., and Yue, S. (2010). Luminescence properties of Sm^{3+}-doped $Sr_3Sn_2O_7$ phosphor. *Mater. Chem. Phys.* 124: 912–915.

88 Liu, Y., Wang, Z., Miao, K. et al. (2022). Research progress on near-infrared long persistent phosphor materials in biomedical applications. *Nanoscale Adv.* 4: 4972–4996.

89 Jia, D., Lewis, L., and Wang, X. (2010). Cr^{3+}-doped lanthanum gallogermanate phosphors with long persistent IR emission. *Electrochem. Solid-State Lett.* 13: J32–J34.

90 Kamimura, S., Xu, C., Yamada, H. et al. (2014). Long-persistent luminescence in the near-infrared from Nd^{3+}-doped Sr_2SnO_4 for in vivo optical imaging. *Jpn. J. Appl. Phys.* 53: 092403.

91 Xu, J., Murata, D., Katayama, Y. et al. (2017). Cr^{3+}/Er^{3+} co-doped $LaAlO_3$ perovskite phosphor: a near-infrared persistent luminescence probe covering the first and third biological windows. *J. Mater. Chem. B* 5: 6385–6393.

92 Liu, F., Liang, Y., Chen, Y., and Pan, Z. (2016). Divalent nickel-activated gallate-based persistent phosphors in the short-wave infrared. *Adv. Opt. Mater.* 4: 562–566.

93 Yang, Y., Wang, K.-Z., and Yan, D. (2017). Lanthanide doped coordination polymers with tunable afterglow based on phosphorescence energy transfer. *Chem. Commun.* 53: 7752–7755.

94 Parker, C.A. and Hatchard, C.G. (1961). Triplet-singlet emission in fluid solutions. Phosphorescence of eosin. *Trans. Faraday Soc.* 57: 1894–1904.

95 Endo, A., Ogasawara, M., Takahashi, A. et al. (2009). Thermally activated delayed fluorescence from Sn^{4+}–porphyrin complexes and their application to organic light emitting diodes- a novel mechanism for electroluminescence. *Adv. Mater.* 21: 4802–4806.

96 Endo, A., Sato, K., Yoshimura, K. et al. (2011). Efficient up-conversion of triplet excitons into a singlet state and its application for organic light emitting diodes. *Appl. Phys. Lett.* 98: 083302.

97 Solov, ev, K.N. and Borisevich, E.A. (2005). Intramolecular heavy-atom effect in the photophysics of organic molecules. *Phys. Usp.* 48: 231–253.

98 Dinh, T.V., Yen, E.L., and Winefordner, J.D. (1976). Heavy-atom effect on room temperature phosphorimetry. *Anal. Chem.* 48: 1186–1188.

99 Yang, S., Wu, D., Gong, W. et al. (2018). Highly efficient room-temperature phosphorescence and afterglow luminescence from common organic fluorophores in 2D hybrid perovskites. *Chem. Sci.* 9: 8975–8981.

100 Ema, K., Inomata, M., Kato, Y. et al. (2008). Nearly perfect triplet-triplet energy transfer from wannier excitons to naphthalene in organic-inorganic hybrid quantum-well materials. *Phys. Rev. Lett.* 100: 257401.

101 Yang, Y., Wang, K.-Z., and Yan, D. (2017). Smart luminescent coordination polymers toward multimode logic gates: time-resolved, tribochromic and excitation-dependent fluorescence/phosphorescence emission. *ACS Appl. Mater. Interfaces* 9: 17399–17407.

102 Mujahid, M.H., Upadhyay, T.K., Khan, F. et al. (2022). Metallic and metal oxide-derived nanohybrid as a tool for biomedical applications. *Biomed. Pharmacother.* 155: 113791.

103 Price, J., Allan, P., and Slater, P. (2023). Optimising the synthesis of $LiNiO_2$: coprecipitation versus solid-state, and the effect of molybdenum doping. *Energy Adv.* 2: 864.

104 Fernández-Arias, M., Vilas, A.M., Boutinguiza, M. et al. (2022). Palladium nanoparticles synthesized by laser ablation in liquids for antimicrobial applications. *Nanomaterials* 12 (15): 2621.

105 Barizão, A., Oliveira, J., Gonçalves, R., and Cassini, S. (2021). Nanomagnetic approach applied to microalgae biomass harvesting: advances, gaps, and perspectives. *Environ. Sci. Pollut. Res.* 28: 1–17.

106 Girija, E., Sekar, K., Duraisamy, K. et al. (2019). Synthesis of NIR emitting rare earth doped fluorapatite nanoparticles for bioimaging applications. *Curr. Phys. Chem.* 09.

107 Makkara, M. and Viswanatha, R. (2018). Frontier challenges in doping quantum dots: synthesis and characterization. *RSC Adv.* 8: 22103–22112.

108 Duraisamy, S., Ganguly, A., Sharma, P.K. et al. (2021). One-step hydrothermal synthesis of phase-engineered MoS_2/MoO_3 electrocatalysts for hydrogen evolution reaction. *ACS Appl. Nano Mater.* 4: 2642–2656.

109 Xu, J., Ueda, J., Kuroishi, K., and Tanabe, S. (2015). Fabrication of Ce^{3+}–Cr^{3+} co-doped yttrium aluminium gallium garnet transparent ceramic phosphors with super long persistent luminescence. *Scr. Mater.* 102: 47–50.

110 Gupta, S.K. and Mao, Y. (2021). A review on molten salt synthesis of metal oxide nanomaterials: status, opportunity, and challenge. *Prog. Mater. Sci.* 117: 100734.

111 Gupta, S.K. and Mao, Y. (2021). Recent developments on molten salt synthesis of inorganic nanomaterials: a review. *J. Phys. Chem. C* 125 (12): 6508–6533.

112 Nag, A. and Kutty, T.R.N. (2003). Role of B_2O_3 on the phase stability and long phosphorescence of $SrAl_2O_4$:Eu,Dy. *J. Alloys Compd.* 354 (1–2): 221–231.

113 Bierwagen, J., Delgado, T., Jiranek, G. et al. (2021). Observation of multiple sites for trivalent europium ions in $SrAl_2O_4$. *J. Lumin.* 222: 117113.

114 Carvalho, J.M., der Heggen, D.V., Martin, L.I.D.J., and Smet, P.F. (2020). Microwave-assisted synthesis followed by a reduction step: making persistent phosphors with a large storage capacity. *Dalton Trans.* 49 (14): 4518–4527.

115 Havasi, V., Tátrai, D., Szabó, G. et al. (2020). On the effects of milling and thermal regeneration on the luminescence properties of Eu^{2+} and Dy^{3+} doped strontium aluminate phosphors. *J. Lumin.* 219: 116917.

116 Relvas, M., Soares, M.R.N., Pereira, S.O. et al. (2019). Trends in Cr^{3+} red emissions from $ZnGa_2O_4$ nanostructures produced by pulsed laser ablation in a liquid medium. *J. Phys. Chem. Solids* 129: 413–423.

117 Srivastava, B.B., Kuang, A., and Mao, Y. (2015). Persistent luminescent sub-10 nm Cr doped $ZnGa_2O_4$ nanoparticles by a biphasic synthesis route. *Chem. Commun.* 51: 7372–7375.

118 Glais, E., Pellerin, M., Castaing, V. et al. (2018). Luminescence properties of $ZnGa_2O_4$:Cr^{3+},Bi^{3+} nanophosphors for thermometry applications. *RSC Adv.* 8 (73): 41767–41774.

119 Srivastava, B.B., Gupta, S.K., Mohan, S., and Mao, Y. (2021). Molten-salt-assisted annealing for making colloidal $ZnGa_2O_4$:Cr nanocrystals with high persistent luminescence. *Chem Eur J* 27 (44): 11398–11405.

120 Mondal, A. and Manam, J. (2020). Structural, optical and temperature dependent photoluminescence properties of Cr^{3+}-activated $LaGaO_3$ persistent phosphor for optical thermometry. *Ceram. Int.* 46: 23972–23984.

121 Srivastava, B.B., Gupta, S.K., and Mao, Y. (2020). Remarkable enhancement of photoluminescence and persistent luminescence of NIR emitting $ZnGa_2O_4$:Cr^{3+} nanoparticles. *CrystEngComm* 22 (14): 2491–2501.

122 Boiko, V., Dai, Z., Markowska, M. et al. (2021). Particle size-related limitations of persistent phosphors based on the doped $Y_3Al_2Ga_3O_{12}$ system. *Sci. Rep.* 11: 141.

123 Zhanga, X., Zhanga, J., Rena, X., and Wanga, X.-J. (2008). The dependence of persistent phosphorescence on annealing temperatures in $CaTiO_3:Pr^{3+}$ nanoparticles prepared by a coprecipitation technique. *J. Solid State Chem.* 181: 393–398.

124 Zhan-Jun, L., Hong-Wu, Z., Meng, S. et al. (2012). A facile and effective method to prepare long-persistent phosphorescent nanospheres and its potential application for in vivo imaging. *J. Mater. Chem.* 22: 24713–24720.

125 Li, Z., Zhang, Y., Wu, X. et al. (2015). In vivo repeatedly charging near-infrared-emitting mesoporous $SiO_2/ZnGa_2O_4:Cr^{3+}$ persistent luminescence nanocomposites. *Adv. Sci.* 2: 1500001.

126 Merízio, L.G., Lodi, T.A., Bonturim, E., and de Camargo, A.S.S. (2022). Persistent luminescent phosphor-in-glass composites based on $NaPO_3–Ga_2O_3$ glasses loaded with $Sr_2MgSi_2O_7:Eu^{2+},Dy^{3+}$. *Opt. Mater.* 134: 113046.

127 Du, J. and Poelman, D. (2020). Red-light-activated red-emitting persistent luminescence for multicycle bioimaging: a case study of CaS: Eu^{2+},Dy^{3+}. *J. Phys. Chem. C* 124 (30): 16586–16595.

128 Heggen, D.V.der., Joos, J.J., and Smet, P.F. (2018). Importance of evaluating the intensity dependency of the quantum efficiency: impact on LEDs and persistent phosphors. *ACS Photonics* 5: 4529–4537.

129 De Clercq, O.Q., Martin, L.I.D.J., Korthout, K. et al. (2017). Probing the local structure of the near-infrared emitting persistent phosphor $LiGa_5O_8:Cr^{3+}$. *J. Mater. Chem. C* 5 (41): 10861–10868.

130 Du, J., De Clercq, O.Q., and Poelman, D. (2019). Temperature dependent persistent luminescence: evaluating the optimum working temperature. *Sci. Rep.* 9 (1): 10517.

131 Gao, Q., Li, C., Liu, Y. et al. (2020). Manipulating trap filling of persistent phosphors upon illumination by using a blue light-emitting diode. *J. Mater. Chem. C* 8: 6988–6992.

132 Van der Heggen, D., Joos, J.J., Rodriguez Burbano, D.C. et al. (2017). Counting the photons: determining the absolute storage capacity of persistent phosphors. *Materials* 10 (8): 867.

133 Li, Y., Li, Y.Y., Sharafudeen, K. et al. (2014). A strategy for developing near infrared long-persistent phosphors: taking $MAlO_3:Mn^{4+},Ge^{4+}$ (M = La, Gd) as an example. *J. Mater. Chem. C* 2: 2019–2027.

134 Abdukayum, A., Chen, J.-T., Zhao, Q., and Yan, X.-P. (2013). Functional near infrared-emitting Cr^{3+}/Pr^{3+} co-doped zinc gallogermanate persistent luminescent nanoparticles with superlong afterglow for in vivo targeted bioimaging. *J. Am. Chem. Soc.* 135: 14125–14133.

135 Bessière, A., Lecointre, A., Priolkar, K., and Gourier, D. (2012). Role of crystal defects in red long-lasting phosphorescence of $CaMgSi_2O_6:Mn$ diopsides. *J. Mater. Chem.* 22: 19039–19046.

136 Zhuang, Y., Chen, D., Chen, W. et al. (2021). X-ray-charged bright persistent luminescence in $NaYF_4:Ln^{3+}@NaYF_4$ nanoparticles for multidimensional optical information storage. *Light Sci. Appl.* 10: 132.